A Szilikátipari Tudományos Egyesület lapja

építőanyag

Journal of Silicate Based and Composite Materials

A TARTALOMBÓL:

2018/4


TUNGSRAM
Innovation is our heritage
EST.1896
INNOVATUNGSRAM
Tungsram returns to the market as an innovative, premium brand with design, development and manufacturing in Europe and a commitment to continue and expand its outreach.
tungsram.com

építőanyag

Journal of Silicate Based and Composite Materials

2018/4

TARTALOM

CONTENT

A finomkerámia-, üveg-, cement-, mész-, beton-, tégla- és cserép-, kő- és kavics-, tűzállóanyag-, szigetelőanyag-iparágak szakmai lapja
Scientific journal of ceramics, glass, cement, concrete, clay products, stone and gravel, insulating and fireproof materials and composites

A folyóiratot referálja · The journal is referred by:
Cambridge Scientific Abstracts
ProQuest

A folyóiratban lektorált cikkek jelennek meg.
All published papers are peer-reviewed.
Kiadó · Publisher: Szilikátipari Tudományos Egyesület (SZTE)
Elnök · President: ASZTALOS István
1034 Budapest, Bécsi út 122–124.
Tel.: +36-1/201-9360 ▪ E-mail: epitoanyag@szte.org.hu
Tördelő szerkesztő · Layout editor: NÉMETH Hajnalka

Címlapfotó · Cover photo: KÓSA Luca Kornélia

WWW.EPITOANYAG.ORG.HU
EN.EPITOANYAG.ORG.HU

Online ISSN: 2064-4477
Print ISSN: 0013-970x
INDEX: 2 52 50 ▪ 70 (2018) 105–132

Vol. 70, No. 4

Effect of firing temperature on triaxial electrical porcelain properties made from Tanzania locally sourced ceramic raw materials

Blasius NGAYAKAMO
MSc Materials Scientist and Engineer at NM-AIST. Department of Materials Energy Science and Engineering. Fields of interest: ceramic raw materials, flux materials and high voltage porcelain insulators.

S. Eugene PARK
Associate Professor and chair, Materials and Energy Science and Engineering at NM-AIST Department of Materials Science and Engineering, Fields of interest: Ceramic and sustainable Energy Engineering.

Blasius NGAYAKAMO ▪ The Nelson Mandela African Institution of Science and Technology, Department of Materials Energy Science and Engineering ▪ henryblasius@gmail.com
S. Eugene PARK ▪ The Nelson Mandela African Institution of Science and Technology, Department of Materials Energy Science and Engineering

Érkezett: 2018. 02. 16. ▪ Received: 16. 02. 2018. ▪ https://doi.org/10.14382/epitoanyag-jsbcm.2018.19

Abstract
The study has investigated the effect of firing temperature during the production of technical triaxial electrical porcelain, for electrical insulation applications using Tanzania locally sourced ceramic raw materials. The green triaxial porcelain samples containing 50 wt% of Pugu kaolin, 35 wt% of Same clay and 15 wt% of feldspar were produced and fired at 1200 °C-1300 °C with a heating rate of 10 °C/min (dwell time of 1.5h) and cooled at 10°C/min to a room temperature. X-ray diffraction technique was used to investigate phases developed in the triaxial electrical porcelain after firing process. The main crystalline phases revealed were mullite and quartz. The technological properties of the triaxial electrical porcelain such as water absorption, apparent porosity, bulk density, bending and dielectric strength were determined for each porcelain sample fired at high temperature. The optimum physical-mechanical and electrical properties were found at 1250°C. However, the triaxial electrical porcelain properties were found to decrease with the increase in firing temperature.
Keywords: Firing temperature, triaxial electrical porcelain, physical-mechanical and dielectric properties
Kulcsszavak: Égetési hőmérséklet, triaxiális szigetelő porcelán, fiziko-kémiai és dielektromos jellemzők

1. Introduction

Triaxial electrical porcelain is composed of clay, feldspar which are locally sourced ceramic raw materials and other filler materials such as quartz and alumina. The raw materials play specific roles in influencing the properties and performance of the final products. Clay [$Al_2Si_2O_5(OH)_4$] provides plasticity, quartz (SiO_2) maintains the shape of the porcelain structure during firing, and feldspar [$KxNa1\text{-}x(AlSi_3)O_8$] promotes vitrification. The three ceramic raw materials place electrical porcelain in the phase system [$(K, Na)_2O\text{-}Al_2O_3\text{-}SiO_2$)] in terms of oxide hence referred as triaxial porcelain [1, 2]. Traditional ceramic raw materials are the potential candidate materials for the production of triaxial electrical porcelains. The use of traditional ceramics as raw materials instead of industrial chemicals is highly preferred due to the lower price of the raw materials [3].

The properties of triaxial electrical porcelain are contributed to the variations in the composition of the raw materials, the method of production, and the firing temperature adopted [1]. The sintered triaxial porcelain product contains mullite ($Al_6Si_2O_{13}$) and undissolved quartz (SiO_2) crystals embedded in glassy phase which result from the liquid phase formed by the melting of feldspar in the raw materials [4].

Therefore the desired properties of triaxial electrical porcelains are achieved particularly during the firing process since the technological properties of clay-based ceramics products depend on firing conditions such as temperature [5, 6]. However, other technological properties which are evaluated to determine the performance of the ceramic product after firing are water absorption, firing shrinkage and bending strength [6]. During the firing process, the triaxial porcelain body undergoes several phase transitions, during which both composition and structure change significantly which influence triaxial porcelain properties at the end of the firing process [5]. Hence, the properties of the triaxial porcelain are mainly influenced by sufficient development of mullite during firing process since the development of mullite in the porcelain is highly associated with firing temperature of the porcelain which should not be below 1150 to 1200 °C for the mullite forming processes to be completed [5, 7]. Therefore, the development of the physical-mechanical and dielectric properties of porcelain are contributed by each phase developed during firing which depends on the concentration and microstructural attributes which are influenced by temperature and the chemical composition of the raw materials which is an important factor because of its effects on porcelain properties [8-11]. Since the effect of firing temperature on the electrical porcelain properties made from Tanzania locally sourced ceramic raw materials is not reported. Therefore, the work intends to evaluate the effect of firing temperature on the triaxial electrical porcelains made from Tanzania locally sourced ceramic raw materials. However, the study focuses also on the phase changes, surface morphology development as well as the physical-mechanical and dielectric properties of the triaxial electrical porcelain sample due to change in firing temperature.

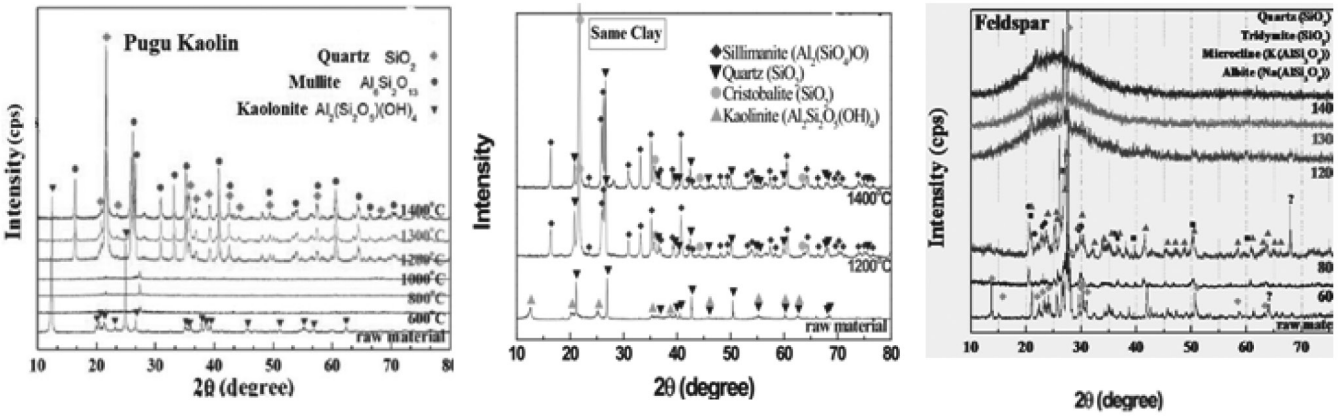

Fig. 1. X-ray diffraction patterns of Pugu kaolin, Same clay and feldspar [16]
1. ábra Pugu kaolin, Same agyag és földpát röntgendiffraktogramjai [16]

2. Experimental procedures

Pugu Kaolin was collected from the Pugu hills, 35 km west of Dar es Salaam, Same clay and feldspar from Same, Kilimanjaro region in the northern zone of Tanzania. The ceramic raw materials were crushed and ball milled to reduce their size. The particle size less than106 µm was achieved by using sieve shaker Model RX-29-10 digit. The chemical composition of the raw materials was analyzed by using X-Ray Fluorescence (XRF) PANalytical, Model: Minipal4 (PW4030)-Rh X-Ray Tube, 30kV, 0.002mA and the results are presented in *Table 1*. The examination of the surface morphology of the porcelain sample was carried out by Scanning Electron Microscope (SEM) Model: JEOL JSM-6335F having a resolution of 10µm at 2kV. The crystalline phase analysis of the porcelain insulator was analyzed by X-ray diffractometer Model: Bruker D2-PHASER-40Kv/44mA. Six triaxial porcelain samples were produced by varying the composition of the locally sourced materials by 50%wt of Pugu kaolin, 35%wt of same clay and 15%wt of feldspar. The powder mixtures were uniaxially compacted into rectangular shapes at 10 MPa. The porcelain green body samples were seasoned at a room temperature for 5 days and they were oven dried at the temperature of 110 °C for 24 hrs. The sintering of porcelain samples was done at 1200, 1250 and 1300 °C for 1.5 hrs at the ramp rate of 10 °C/min in each firing process. The sintered porcelain bodies were left to cool at 10 °C/min to room temperature and were subjected to physical-mechanical properties and dielectric strength analysis.

3. Results and discussion

3.1 Chemical composition of the raw materials

The chemical compositions of the raw materials in form of their oxides are presented in *Table 1*. The study results reveal that both clays have the higher content of silica and alumina. However, feldspar and Pugu kaolin have a higher content of Hematite (Fe_2O_3) compared to Same clay. The literature reports that small amount of coloring oxides such as Fe_2O_3 and TiO_2 less than 0.9% may be accepted for porcelain wares production [12]. However, a considerable high amount of Fe_2O_3 in Pugu kaolin and feldspar may not be accepted as they may impart yellowish and reddish color in porcelain wares unless beneficiated. Feldspar has considerable higher alkaline oxide K_2O than Pugu kaolin and Same clay. During the sintering process, the alkaline oxide K_2O melts and forms the liquid phase that contributes to densification at higher temperatures due to the formation of the glassy phase. Nevertheless, the quantities of the alkaline oxides depend on the mineralogical nature of the clays and their reactivity during melting of the clay minerals [13]. The alkaline oxides(K_2O and Na_2O) play a significant role towards vitrification, phase transformation and mullite grain growth [14, 15].

Oxides	Pugu kaolin	Same clay	Feldspar
SiO_2	60.0	60.4	57.1
Al_2O_3	30.3	13.9	14.0
Fe_2O_3	3.95	1.40	3.08
MnO	0.021	0.00	0.32
CaO	0.39	0.00	1.0
Na_2O	0.00	0.04	0.20
K_2O	2.14	2.6	12.09

Table 1. Chemical composition of raw materials
1. táblázat Alapanyagok kémiai összetétele

3.2 Mineralogical composition of the raw materials

The X-ray diffraction patterns of the ceramic raw materials before and after firing are presented in *Fig. 1* as reported by [16]. The result shows phase compositions of both Pugu kaolin and Same clay are kaolinite, however, Pugu kaolin showed the development of crystalline phases of mullite and quartz at a temperature of 1400 °C. In addition, Same clay was observed to form cristobalite and sillimanite above 1200 °C. Feldspar contains albite, and microcline, tridymite, and quartz. Since the major components of interests are potassium feldspar ($K_2O{\cdot}Al_2O_3{\cdot}O{\cdot}6SiO_2$) sodium feldspar ($Na_2O{\cdot}\ Al_2O_3{\cdot}O{\cdot}6SiO_2$); and lime feldspar ($CaO{\cdot}Al_2O_3{\cdot}O{\cdot}6SiO_2$). However, the results indicate that feldspar deposit contains a high content of potash feldspar compared to soda feldspar which is also supported by the chemical composition by XRF that is K_2O is 12.09% while

Na_2O is only 0.20%.So feldspar deposit is, therefore, a potash feldspar. Feldspar promotes vitrification of the porcelain insulator at the end of the sintering process.

3.2 Characterization of fired triaxial porcelain samples

Fig. 2 presents the results of water absorption, apparent porosity, and bulk density respectively for the porcelain samples versus firing temperature. The figure shows that the best values for physical properties for triaxial electrical porcelain are achieved at the firing temperature of 1250 °C. This might be due to the formation of the liquid phase and densification at this firing range. However, the values of water absorption, apparent porosity, and bulk density were observed to decrease at higher firing temperature. This might be due to the expansion of trapped water bubbles inside the porcelain matrix and change in the composition of the glassy phase [1, 3]. The results of the study are in agreement with the works of [1, 3, 13]. The authors reported that water absorption and bulk density increased due to vitrification and densification of the porcelain samples. However, the physical properties were observed to vary due to the decrease of vitrification range and an increase of firing temperature due to the expansion of trapped water bubbles inside the porcelain sample at high firing temperatures. Generally, the variation of the physical properties of the triaxial electrical porcelain might have been caused by the method of production, chemical and mineralogical properties of the raw materials.

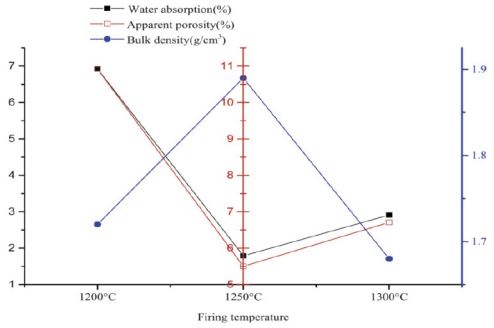

Fig. 2. Physical properties of triaxial electrical porcelain sample versus firing temperature
Fig. 2. Triaxiális szigetelő porcelán fizikai jellemzői az égetési hőmérséklet függvényében

Fig. 3 shows changes in the mechanical strength of triaxial electrical porcelain with firing temperature. The trend shows that the increase of mechanical strength of porcelain sample may be due to increased densification, vitrification and in absence of microcracks. The best mechanical strengths (both bending and compressive strengths) were obtained at 1250 °C. However, the mechanical strengths began to decrease above 1250 °C due to closed pores development and a considerable amount of cracks on the surface of the porcelain samples. The results of the current study are in agreement with the previous studies as reported in the works of Kitouni *et al.*,[13] and Olupot *et al.,* [1]. The authors have reported that the mechanical strength increases due to increased densification with temperature and tends to decrease due to development of pores at high firing temperature. However, the mechanical strength was found to decrease with the increase of the firing temperature due expansion of closed pores and microcracks [1]. Hence the mechanical strength of a porcelain sample is strongly dependent on the defects such as pores and cracks [13].

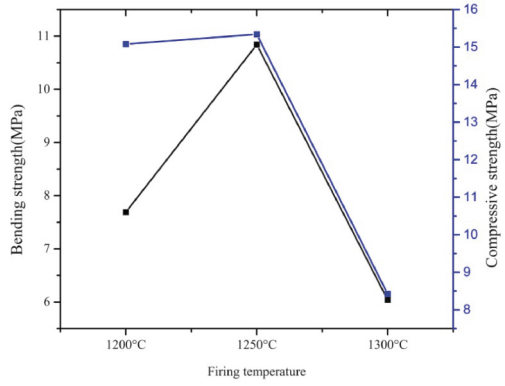

Fig. 3. Variation of mechanical strength of triaxial electrical porcelain sample versus firing temperature
Fig. 3. Triaxiális szigetelő porcelán mechanikai jellemzői az égetési hőmérséklet függvényében

Fig. 4 shows the variation of the dielectric strength of porcelain samples fired at 1200, 1250 and 1300 °C. The trend shows that the dielectric strength increases with an increase in firing temperature and began to decrease with further temperature rise at 1300 °C. The increase of the dielectric strength of electrical porcelains is due to increased vitrification range of the electrical porcelains samples. The results of the current study are also reported by Olupot *et al,* [1]. The authors evaluated ceramic raw materials from Uganda for electrical porcelain production. The authors obtained the highest dielectric strength of 19kV/mm at 1250 °C. However, above 1250 °C, the samples became more porous due to change in the composition of the glassy phase. The dielectric strength was found to decrease with the increase of firing temperature which affected vitrification range and the dielectric properties of the triaxial electrical porcelain.

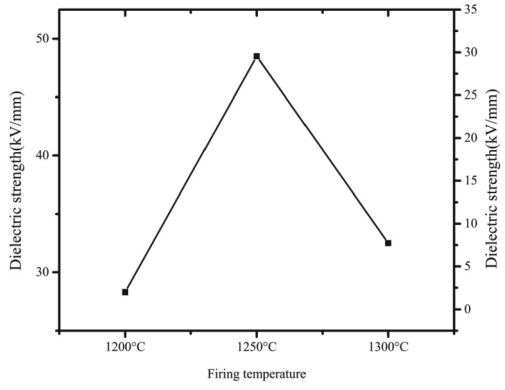

Fig. 4. Variation of dielectric strength of triaxial electrical porcelain sample versus the firing temperature
Fig. 4. Triaxiális szigetelő porcelán dielektromos jellemzői az égetési hőmérséklet függvényében

In *Fig. 5* the X-diffraction pattern of triaxial electrical porcelain is presented. The diffractogram confirms that the mullite and quartz phases are present in the porcelain insulator. Both phases promote the mechanical and dielectric properties

of the porcelain insulator. However, high peaks of quartz may lead to high amount of glassy phase which may lower the dielectric strength of the porcelain insulators but not the mechanical strength of a porcelain insulator which is affected by microcracks. The high amount glassy phase provides free movement of mobile ions such as Na^+, K^+, and Al^{3+} which increases the conductivity [17].

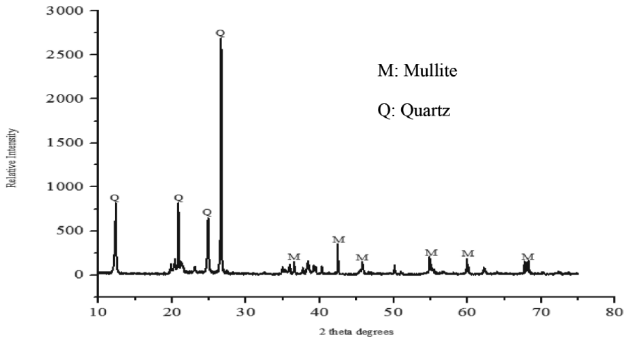

Fig. 5. X-ray diffraction pattern of a porcelain insulator fired at 1250 °C
Fig. 5. 1250 °C hőmérsékleten égetett szigetelő porcelán röntgendiffraktogramja

Fig. 6 shows the examination of the surface morphology using the Scanning Electron Microscope (SEM) Model: JEOL JSM-6335F having a resolution of 10nm at 2kV. It was evidenced the densification on the surface of the triaxial electrical porcelain sample after the firing process was completed.

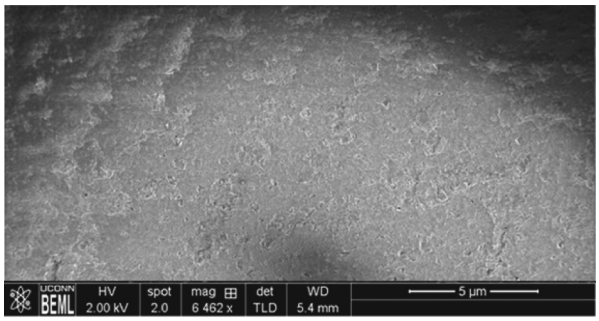

Fig. 6. SEM micrographs showing densification of triaxial electrical porcelain sample at 1250 °C
Fig. 6. 1250 °C hőmérsékleten égetett triaxiális szigetelő porcelán elektronmikroszkópos felvétele

4. Conclusions

In this research work, the effect of firing temperature on triaxial porcelain samples properties was investigated. At the optimum firing temperature of 1250 °C, the best physical-mechanical and dielectric properties were achieved. However, firing beyond 1250 °C resulted in progressive deterioration of the physical-mechanical and the dielectric properties of the electrical porcelain samples. This might have been caused by the development of microcracks and high content of glassy phase caused by high peaks of quartz. So it is imperative to be aware that, the actual firing temperature and its influence on the triaxial electrical porcelain properties depend on the chemical composition of the materials under study. Therefore, the locally sourced materials need to be evaluated from time to time in order to avoid deviation of the desired triaxial electrical porcelain properties during the firing process.

References

[1] Olupot, P. W. (2006): Assessment of ceramic raw materials in Uganda for electrical porcelain, *KTH*.
[2] Carty, W. M. – Senapati, U. (1998): Porcelain—raw materials, processing, phase evolution, and mechanical behavior. *Journal of the American Ceramic Society*, 1998. 81(1): p. 3-20. https://doi.org/10.1111/j.1151-2916.1998.tb02290.x
[3] Kasrani, S., et al., (2016): Sintering and dielectric properties of a technical porcelain prepared from economical natural raw materials, *Cerâmica,* 2016. p. 405-412. https://doi.org/10.1590/0366-69132016623641994
[4] Olupot, P. W. – Jonsson, S. – Byaruhanga, J. K. (2013): Effects of the Sintering Process on Properties of Triaxial Electrical Porcelain from Ugandan Ceramic Minerals. *World Academy of Science, Engineering and Technology, International Journal of Chemical, Molecular, Nuclear, Materials and Metallurgical Engineering*, 2013. 7(5): p. 267-273. http://scholar.waset.org/1307-6892/11565
[5] Stubna, I. – Sin, P. – Viljus, M. – Trnik, A. (2014): The effect of the firing temperature on the hardness of alumina porcelain. *Materiali in tehnologije*, 2014. 48(3): p. 331-336. http://mit.imt.si/Revija/izvodi/mit143/stubna.pdf
[6] Njoya, D. – Tadjuidje, F. S. – Ndzana, E. J. A. – Pountouonchi, A. – Tessier-Doyen, N. – Lecomte-Nana, G. (2017): Effect of flux content and heating rate on the microstructure and technological properties of Mayouom (Western-Cameroon) kaolinite clay-based ceramics. *Journal of Asian Ceramic Societies,* 2017. 5(4): p. 422-426. https://doi.org/10.1016/j.jascer.2017.09.004
[7] Jang-Hoon Ha – Jongman Lee – In-Hyuck Song – Sang-Hyup Lee (2015): The effects of diatomite addition on the pore characteristics of a pyrophyllite support layer. *Ceramics International,* 2015. 41(8): p. 9542-9548.
[8] Olupot, P. W. – Jonsson, S. – Byaruhanga, J. K. (2008): Effects of mixing proportions and firing temperature on properties of electric porcelain from Ugandan minerals. *Industrial Ceramics*, 2008. 28(1): p. 1-10.
[9] Iqbal, Y. – Lee, W. E. (2000): Microstructural evolution in triaxial porcelain. *Journal of the American Ceramic Society,* 2000. 83(12): p. 3121-3127. https://doi.org/10.1111/j.1151-2916.2000.tb01692.x
[10] Lee, W. – Iqbal, Y. (2001): Influence of mixing on mullite formation in porcelain. *Journal of the European Ceramic Society*, 2001. 21(14): p. 2583-2586. https://doi.org/10.1016/S0955-2219(01)00274-6
[11] Chaudhuri, S. – Sarkar, P. – Chakraborty, A. (1999): The Electrical resistivity of porcelain in relation to the constitution. *Ceramics International,* 1999. 25(1): p. 91-99. https://doi.org/10.1016/S0272-8842(98)00006-6
[12] Acchar, W. – Dultra, E. J. (2015): Ceramic Materials from Coffee Bagasse Ash Waste. 2015: *Springer*.
[13] Kitouni, S. – Harabi, A. (2011): Sintering and mechanical properties of porcelains prepared from Algerian raw materials. *Cerâmica*, 2011. 57(344): p. 453-460. https://doi.org/10.1590/S0366-69132011000400013
[14] Chaudhuri, S., (1974): Influence of mineralizers on constitution of hard porcelain. 1. Mineralogical compositions. *American Ceramic Society Bulletin*, 1974. 53(2): p. 169-171.
[15] Das, S. K. – Dana, K. (2003): Differences in densification behavior of K-and Na-feldspar-containing porcelain bodies. *Thermochimica Acta,* 2003. 406(1): p. 199-206. https://doi.org/10.1016/S0040-6031(03)00257-0
[16] Hamisi, H., et al., (2014): Influence of firing temperature on physical properties of same clay and Pugu kaolin for ceramic tiles application. *International Journal of Materials Science and Applications*, 2014. 3(5): p. 143-146. https://doi.org/10.11648/j.ijmsa.20140305.12
[17] Islam, R. A. – Chan, Y. – Islam, M. F. (2004): Structure-property relationship in high-tension ceramic insulator fired at high temperature. *Materials Science and Engineering: B,* 2004. 106(2): p. 132-140. https://doi.org/10.1016/j.mseb.2003.09.005

Ref.:
Ngayakamo, Blasius – **Park**, S.Eugene: *Effect of firing temperature on triaxial electrical porcelain properties made from Tanzania locally sourced ceramic raw materials*
Építőanyag – Journal of Silicate Based and Composite Materials, Vol. 70, No. 4 (2018), 106–109. p.
https://doi.org/10.14382/epitoanyag-jsbcm.2018.19

Anisotropic response of the Holzapfel's constitutive model for the lumbar spine considering degenerative conditions

Moustafa MOSBAH ▪ Laboratory of numerical and experimental modeling of mechanical phenomena, Department of Mechanical Engineering, University Abd El Hamid Ibn Badis of Mostaganem, Algeria

Mohammed BENDOUKHA ▪ Laboratory of numerical and experimental modeling of mechanical phenomena, Department of Mechanical Engineering, University Abd El Hamid Ibn Badis of Mostaganem, Algeria▪ bendoukham@yahoo.fr

Érkezett: 2018. 02. 26. ▪ Received: 26. 02. 2018. ▪ https://doi.org/10.14382/epitoanyag-jsbcm.2018.20

Abstract

In order to study the risk of disc degeneration under load carriage, an osseo ligamentous FE model of the L4-L5 segment extracted from the validated lumbosacral model L1/S1 was used. Starting from CT images to simplified geometry, many programs and codes were used to simplify the geometry, assemble the mesh and formulate the bony structures of the segment. Abaqus 6.14 was used to pre and post analysis of the FE-model, which included a detailed calibrated model of intervertebral disc (IVD), The range of motion (ROM) curves, the intradiscal pressure, load-strain amount under pure physiological loads were considered for investigation. The model developed in this study considered the holzapfel anisotropy hyperelasticity of the annulus as well as a realistic description of the nucleus geometry, which allowed an improved representation of in vitro and in vivo experimental data during the validation process.

Keywords: intervertebral disc, L4-L5, range of motion finite element model, CT images, intradiscal pressure, Holzapfel anisotropy, hyperelasticity

Kulcsszavak: intervertebrális lemez, L4- L5, mozgásterjedelem végeselemes modellje, CT felvétel, intradiszkális nyomás, Holzapfel anizotrópia, hiperelaszticitás

Moustafa MOSBAH
PhD candidate in biomechanics under the supervision of Dr. BENDOUKHA at the laboratory of numerical and experimental modeling of mechanical phenomena. Obtained the licence and Master's degree from the University of Mostaganem in Mechanics.

Mohammed BENDOUKHA
Research Professor at the University of Mostaganem. Obtained his Engineering degree in Mechanical Engineering from the University of Science and Technology of Oran (USTO). After postgraduation studies he obtained Magister at the USTO IN 1991. Obtained his PhD in tribology speciality in 2010 at the University of Mostaganem, and subsequently his habilitation to direct the research of the same university in 2011. He is active in the field of research at the laboratory of numerical and experimental modeling of mechanical phenomena.

1. Introduction

The disc degeneration is characterized by changes in the morphology and biochemistry of the IVD [16]. These biologic changes of disc degeneration are associated with back pain and other spinal disorders, such as disc herniation, spondylolisthesis, facet arthropathy, and stenosis. FE method is able to simulate a variety of clinical situations in a more way, and has been acting a fully matching partnership based on experimental approaches for spine biomechanics research [12]. The FE-models are widely used to provide an assessment of spine with spinal instrumentation and assist in the design, development and optimization of that spinal instrumentation. Advanced to other methods, these FE-models can predict the changes of stresses and strains in the IVD, vertebrae and ligaments and very comprehensive ROM data [8, 20]. Our main objective is to review the most recent computational studies in the application of FE models that report the issue of research better understanding of low back pain and eventually treat the spinal disorders. Little experiments were performed on intact motion segments (Miller 1986, Lin 1978, Hirsch & Nachemson 1954) and some on FSUs without posterior elements [2, 10, 13]. In the compression load case, the data from Brown 1957 is slightly lower than the generated values and the other experimental data. Some FE-models simulate the effects of degeneration [16], by simply removing some elements from the annulus fibrosus. Where others [18, 19, 20] disclose the influence of geometrical, mechanical, or poromechanical parameters on IVD behavior without showing change in mechanical properties of degenerated IVD. More recently, recent poroelastic finite element model of the lumbar spine was developed to assess spinal response during physiological functions and behavior of degenerative disc [15, 16].

2. Methods and materials

A three-dimensional finite element (FE) model of the L4-5 FSU segment (*Fig. 2*) by modifying the mechanical properties of the intervertebral disc constituents [3]. All the bony structures including cortical and trabecular bone, whereas facet cartilage layers, annulus ground substance, nucleus pulposus and cartilage endplates were modeled by using solid hexahedral elements. The nucleus pulposus composed 43% of the whole volume of the disc. The symmetric FE-model of the human lumbar disc is developed to investigate the optimized properties required to mimic the intact by matching model predictions to experimental results. Facet joints simulated by a cartilaginous layer extruded in Abaqus along the vectors normal to the inferior face of the superior articular process to the central of thickness of 0.4 mm were modeled to be multi-linear elastic in compression [19] by surfaces-to surface contact with softened contact in the normal direction. [20] An initial typically gap of 0.2 mm was specified as reported [20]. The seven major ligaments were modeled as three dimensional, 4 noded Quad elements (T3D2) and allocated were as piecewise linear functions in stress-strain relationship [7, 8] as shown in *Table. 1*. This formulation allows simulation of changing ligament characteristics with different stress at a different level as a function of stress-strain.

Part	Structure	Young's modulus E (MPa)					Poisson's ratio υ	Element type	Reference
Vertebrae	Trabecular bone	100					0.2	C3D8	[8, 14]
	Cortical bone	12,000					0.3		[8]
	Posterior element	3,500					0.25		[8, 14]
	Cartilaginous End plate	23.8					0. 4		[20]
	Facet cartilage	11					0.4		[5, 20]
	Facet contact	Nonlinear soft contact						Contact	[21,22]
Annulus Fibrosus		C_{10}	C_{20}	K1	K2	kappa			
	Healthy	1.5715	9.2044	12.2	39.7	0.113		C3D8	[22]
	Degenerated	1	8.6	18.56	82.31	0.226			
Nucleus Pulposus	Healthy	Incompressible fluid						F3D4	[6, 19, 21]
	Degenerated	compressible fluid							
Ligaments		Nonlinear stress-strain curve						S4R	[7, 8, 21]

Table 1. Material properties used in FE Model
1. táblázat A végeselemes modellben használt anyagjellemzők

The entire model consists of approximately 424 S4R shell elements and 33360 hexahedral elements C3D8

2.1 The intervertebral disc (IVD)

The intervertebral disc was modeled using two separate structure (*Figs. 2* and *5*).

2.2 The Nucleus Pulposus (NP)

The Nucleus Pulposus (NP) exhibits a gelatinous core and, therein describes the mutually coupled behavior of both solid deformation and viscoelastic characteristics of fluid flow [7]. An initial hydrostatic pressure of 0.1 MPa was prompted in the fluid filled cavity in the nucleus pulposus to simulate unloaded motion segments (*Fig. 2*) [17]. The healthy nucleus pulposus was modeled as incompressible fluid while the degenerated nucleus was defined as compressible fluid [10]

2.3 The Annulus Fibrosus (AF)

The Annulus Fibrosus (AF) was modeled as an anisotropic continuum structure, with deformation tensor [8], and the material coefficients C_{10}, C_{20}, k_1, k_2 and κ were based on biaxial tension tests performed on healthy and degenerated annuli fibrosi [9]. The progression of degeneration was simulated using three model variants:

$$W_{matrix} = C_{10}\,(I_1 - 3) + C_{20}\,(I_1 - 3)^2 \quad (1)$$

$$W_{fibers} = \frac{k_1}{2k_2} \sum_{\alpha=4,6} \left(e^{k_2\,[(1-\kappa)(I_1-3) + \kappa(I_\alpha - 1)]^2} - 1 \right) \quad (2)$$

The human healthy and degenerated intervertebral disc.were modeled using three structures:

(a) Healthy intervertebral disc (grade I) defined by healthy annulus and healthy nucleus;

(b) Moderate degeneration disc (grade III) defined by healthy annulus and degenerated nucleus;

(c) Severe degeneration disc (grade IV) defined by degenerated annulus and degenerated nucleus. The grading is based on the Thompson degeneration scale *Fig. 1*.

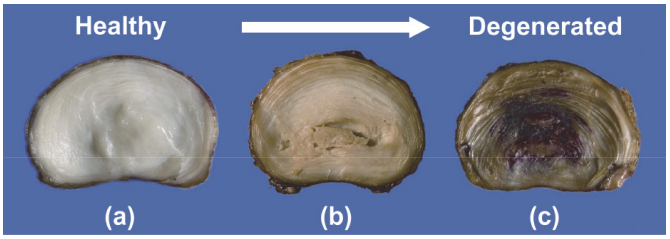

Fig. 1. (a) Healthy intervertebral discs; (b) moderate degeneration; (c) severe degeneration [23]
1. ábra (a) Egészséges intervertebrális lemez; (b) közepes mértékű károsodás; (c) súlyos károsodás [23]

3. Model formulation

The algorithms proposed in the present study is implemented into Abaqus as a User Material UMAT code embedded in an Python and Intel Fortran Compiler environment to simulate the biomechanical behavior of Annulus. This numerical approach consists on Holzapfel's hyperelastic constitutive models of the Annulus and a constitutive model of the seven major Ligaments, which were implemented in Abaqus via subroutines. The coefficients employed in all three conditions are listed in Table 1. While the material properties and in situ nuclear pressure were altered, osteophytes, local tears or similar macroscopic abnormalities were not modeled. Rather than attempting to simulate these defects of an independent individual and random nature, the focus was kept on the effects of measured changes in tissue behavior.

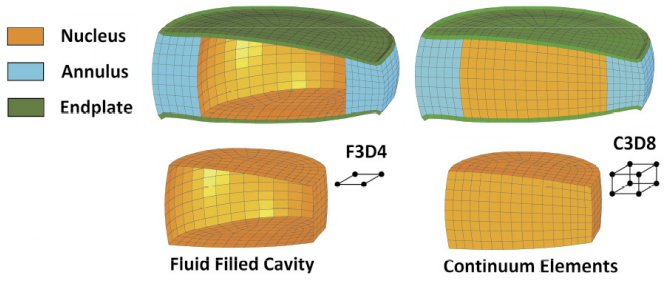

Fig. 2. Finite Element Model of the Intervertebral Disc IVD
2. ábra Intervertebrális lemez IVD végeselemes modellje

4. Loading and Boundary Conditions

The IVD model comprises the intervertebral disc and the adjacent vertebral bodies. The lower vertebral body was rigidly fixed. Pure unconstrained axial compressive of 2000 N was applied to the upper vertebral body to the reference point which coupled all points on upper surface of the disc. The resulting stress-strain distribution at the center of the disc were estimate and the intradiscal Pressure IDP was predicted using the cavity point. Theoretically speaking, we used the concept of nucleus pulposus pressure measurement; by means of in vitro experiments on vertebra-disc-vertebra preparation whither, we found that the incompressible fluid pressure within the nucleus is directly related to the axial compression applied to the disc. The lower portion of the L5 vertebral body and its inferior facets were rigidly fixed. The load was applied through a reference node constrained to the upper surface of the L4 vertebrae using Abaqus Coupling Constraints elements (CCE). The L4/L5 Functional Spinal Unit (FSU) move in six different directions (six degrees of freedom (DOF)). A pure bending moment was incrementally increased 0, 1, 2.5, 5, 7.5, 10 Nm and applied to the model in all three planes of motion.

5. Results

5.1. ROM results

The finite element model predicted an increase in hydrostatic stress in the middle regions of the annulus by nearly seven fold. The intradiscal pressure IDP is considered to be very significant component to approximate internal stress behavior of the intervertebral disc. The in vitro measurements of the nucleus pressure in human intervertebral discs have shown proportion between IDP pressure and applied Load on the superior surface motion (ROM) in all loading directions except for lateral bending comparing to experimental.

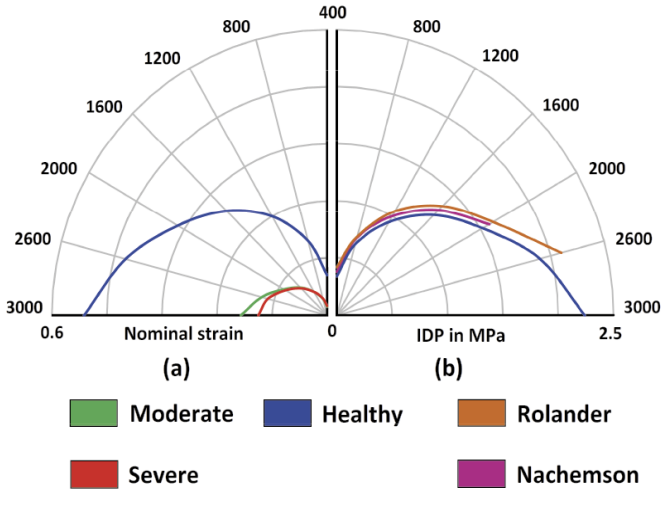

Fig. 3. (a) Comparison of intradiscal pressure (IDP) of the Healthy model with experimental results (b) Comparison of nominal strain of fibers against the Load (N) of Healthy, Moderate and Severe models
3. ábra (a) Kísérleti intradiszkális nyomás (IDP) összehasonlítása az egészséges modell alapján számított értékkel; (b) Szálmegnyúlás és terhelőerő összehasonlítása egészséges, közepes és súlyos modellben

The greatest changes between Healthy and Moderate and Severe models were predicted in axial rotation by 30 % and 36 %. In lateral bending, a 27% increase in ROM was predicted in the Severe scenario (with respect to the Healthy condition), while the change in the Moderate scenario was approximately 32% (*Fig. 4*).

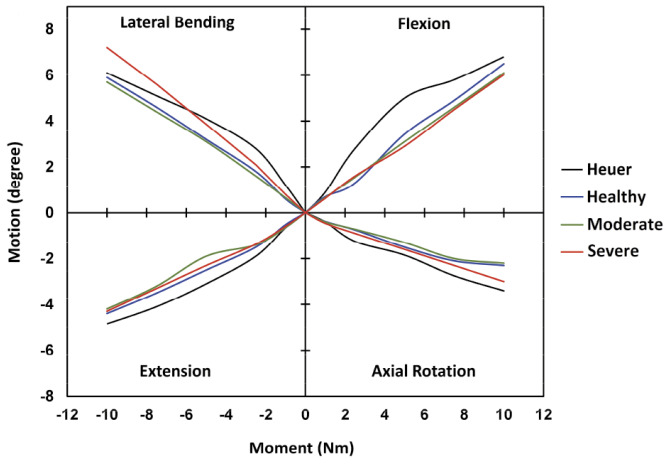

Fig. 4. ROM of L4-L5 FSU
4. ábra L4-L5 funkcionális szegmentális egység (FSU) mozgásterjedelme (ROM)

5.2. Stress and strain results

The analysis of the stress results allowed us to prove the most loaded region. As a most critical region for of spinal diseases, the presence of disc degeneration under physiological load steer to the alteration of the spine comportment and the pain function. The results for the body functions (*Figs. 5-6*) indicate that the superior values of the stresses were situated at posterior region which reaches stress of 2.9 MPa for healthy disc and 2.4 MPa for the degenerated disc; as expected, the results highlight that the most risky load condition corresponds to posterior side. For the degenerated nucleus the results presented in Moderate degeneration a decreased stress according to strain decreasing comparing to Healthy IVD. Furthermore, the magnitude of stress predictions were reduced in the anterior region of the disc while they increased in the posterior region as the simulated degeneration progressed. In all cases, the highest stresses were concentrated in the posterior region of the disc in extension loading. The highest strain were concentrated in the posterolateral region of the disc in lateral bending loading as degeneration progressed (Healthy-Moderate-Severe). The compressive strain prediction in the annulus increased in anterior extremities in extension and in the posterior extremities in flexion *Fig. 5*.

6. Discussion

The aim of this work was to construct an accurate FE-model to characterize the mechanical behavior of healthy and degenerated IVD. This model takes into account the IVD nature and also the clear preferential orientation of the collagen fibers in the annulus. The reduction in nonlinearity behavior with degeneration could suggest a diminished compaction effect of the degenerate tissues at large deformations which could be related to structural changes in annulus. The obtained

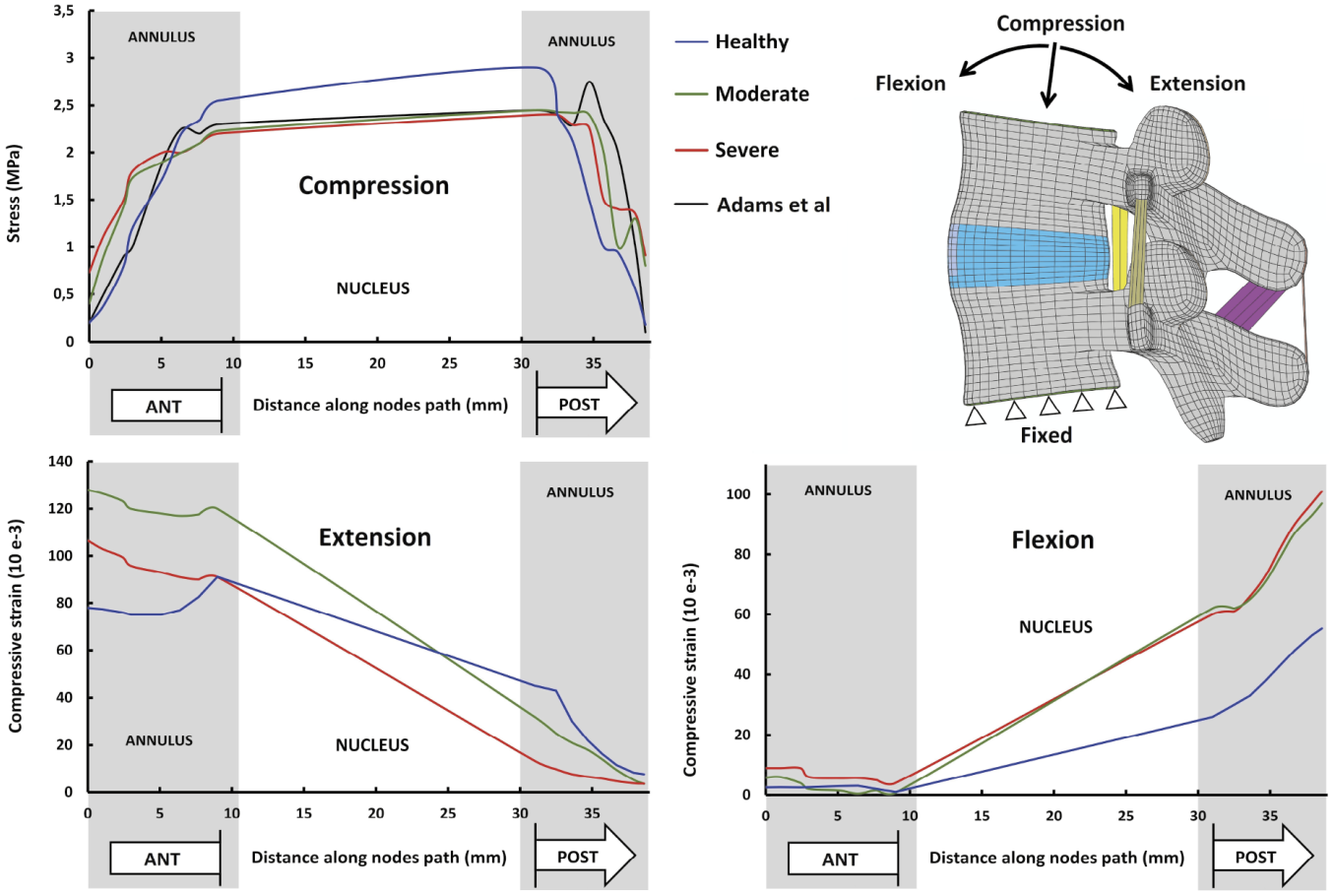

Fig. 5. Axial stress distribution and compressive strain predictions obtained from FE Models in the mid-height plane of the IVD from posterior to anterior midline under Compression (2000 N), Flexion and Extension (10 Nm).

5. ábra Tengelyirányú feszültségeloszlás és összenyomódás a végeselemes modell alapján az intervertebrális lemez középsíkjában, a posteriorból az anteriorba, nyomás (2000 N), hajlítás és megnyúlás (10 Nm) hatására

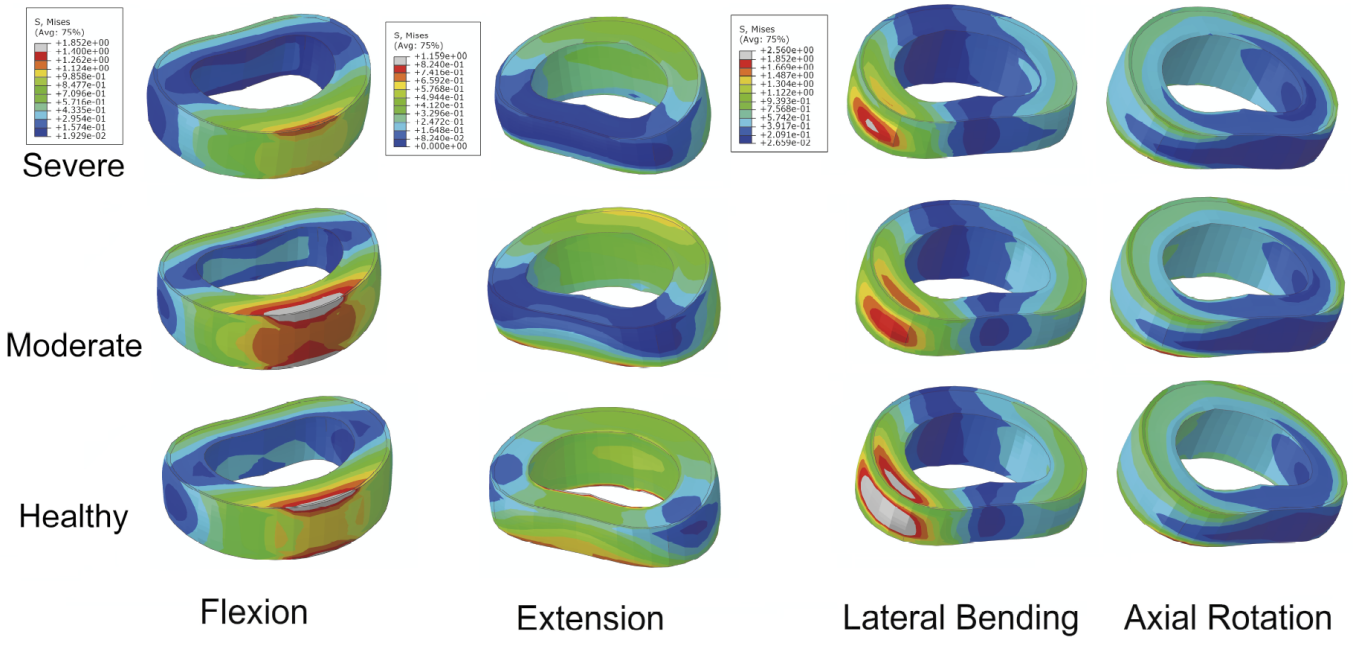

Fig. 6. Von-Mises Stress distribution obtained from FE Models: Healthy, Moderate, Severe

6. ábra Von-Mises feszültségeloszlás a végeselemes modell alapján egészséges, közepes és súlyos modellben

results are also in agreement with the experimental behavior [9, 20]. Experimental results, showed an increase of the elastic modulus in the toe part, thus there is a big role of fibers therefore when the fibers act there is no additional stiffening. In this analysis it has been obtained that the degeneration affects the biomechanics of this FSU; in particular an increase of the ROM in extension and partial decrease in flexion and lateral bending has been noticed.

7. Conclusions

In conclusion, the developed FE-model is capable of generating the mechanical behavior of normal and degenerated NP tissue with a favorable approximation. But on the degeneration of the other segments is a very complex procedure which should be identified in the degeneration of the AF tissue with accurate mechanical properties. Furthermore, the current work provides a qualitative analysis of the influence of single level disc degeneration on the mechanics of the segments under flexion/extension, lateral bending and axial rotation moments. It has been seen that degeneration modified the degree of motion and loading of the degenerated level. These changes could increase the risk of progression of degeneration to the nearest segments of the spine. The results obtained with the FE model seem to be in good agreement with in-vitro data as showed in *Figs. 2* to *4*. Additionally, nonlinear analytical functions used in the IVD ligaments facet joint may be used as input data to perform more accurate computational simulations of the full lumbosacral spine.

References

[1] Berkeston, M – Schultz, A. B. (1979): Mechanical properties of human lumbar spine motion segments: II. Response in compression and shear; influence of gross morphology. *Journal of Biomechanical Engineering 1979*; 101:53–7. https://doi.org/10.1115/1.3426225

[2] Brown, T. – Hansen, R. J. – Yorra, A. J. (1957): Some mechanical tests on the lumbosacral spine with particular reference to intervertebral discs; a preliminary report. *The Journal of Bone and Joint Surgery* 1957, 39:1135–1164.

[3] Chazal, J. – Tanguy, A. – Bourges, M. – Gaurel, G. – Escande, G. – Guillot, M. (1985): Biomechanical properties of spinal ligaments and a histological study of the supraspinal ligament in traction, *Journal of Biomechanics 18,* 167-176, 1985. https://doi.org/10.1016/0021-9290(85)90202-7

[4] Chen, S. H. – Chiang, M. C. – Lin, J. F. – Lin, S. C. – Hung, C. H. (2013): Biomechanical comparison of three stand-alone lumbar cages--a three-dimensional finite element analysis. *BMC Musculoskelet Disord.* https://doi.org/10.1186/1471-2474-14-281

[5] Denoziere, G. – Ku, D. N. (2006): Biomechanical comparison between fusion of two vertebrae and implantation of an artificial intervertebral disc, *Journal of Biomechanics*, 39(4), 766-775. https://doi.org/10.1016/j.jbiomech.2004.07.039

[6] Dreischarf, M – Zander, T. – Shirazi-Adl, A. – Puttlitz, C. M. – Adam, C. J. – Chen, C. S. – Goel, V. K. – Kiapour, A. – Kim, Y. H. – Labus, K. M. – Little, J. P. – Park, W. M. – Wang, Y. H. – Wilke, H. J. – Rohlmann, A. – Schmidt, H. (2014): Comparison of eight published static finite element models of the intact lumbar spine: Predictive power of models improves when combined together, *Journal of biomechanics*, Vol.47, No. 8, pp. 1757–1766, 2014. https://doi.org/10.1016/j.jbiomech.2014.04.002

[7] Eberlein, R. – Holzapfel, G. A. – Schulze-Bauer, C. A. J. (2001): An anisotropic model for annulus tissue and enhanced finite element analyses of intact lumbar disc bodies. *Computer Methods in Biomechanics and Biomedical Engineering 2001*;4(3):209–29 https://doi.org/10.1080/10255840108908005

[8] Goel, V. K. – Monroe, B. T. – Gilbertson, L. G. – Brinckmann, P. (1995): Interlaminar shear stresses and laminae separation in the disc. *Finite element analysis of the L3-L4 motion segment subjected to axial compressive loads*. Spine, 20(6), 689-698.

[9] Heuer, F. – Schmidt, H. – Klezl, Z. – Claes, L. – Wilke, H. J. (2007): Stepwise reduction of functional spinal structures increase range of motion and change lordosis angle, *Journal of Biomechanics 40*, 271- 280, 2007 https://doi.org/10.1016/j.jbiomech.2006.01.007

[10] Hirsch, C. – Nachemson, A. (1954): New Observations on the mechanical behavior of lumbar discs. *Acta Orthopaedica Scandinavica 23* (4), 254–283. https://doi.org/10.3109/17453675408991217

[11] Stokes, I. A. – Iatridis, J. C. (2004): Mechanical conditions that accelerate intervertebral disc degeneration: overload versus immobilization, *Spine*, Vol.29, No.23, pp.2724–2732, 2004.

[12] Urban, J. P. – Maroudas, A. – Bayliss, M. T. – Dillon, J. (1979): Swelling pressures of proteoglycans at the concentrations found in cartilaginous tissues, *Biorheology*, Vol.16, No.6, pp.447–464,1979. https://doi.org/10.3233/BIR-1979-16609

[13] Lin, H. S. – Liu, Y. K. – Adams, K. H. (1978): Mechanical response of the lumbar intervertebral joint 627 under physiological (complex) loading. *The Journal of Bone and Joint Surgery 60A* (1), 41-55.

[14] Lu, Y. M. – Hutton, W. C. – Gharpuray, V. M. (1996): Do bending, twisting, and diurnal fluid changes in the disc affect the propensity to prolapse? A viscoelastic finite element model. *Spine* Nov 1996, 21(22):2570–2579.

[15] Luoma, K. – Riihimaki, H. – Luukkonen, R. (2000): Low Back Pain in Relation to Lumbar Disc Degeneration. *Spine*, Vol. 25, No. 4, pp. 487-492

[16] Adams, M. A. – Roughley, P. J. (2006): What is intervertebral disc degeneration, and what causes it? *Spine*, Vol.31, no.18, pp. 2151–2161, 2006.

[17] Markolf, K. L. (1972): Deformation of the thoracolumbar intervertebral joints in response to external loads. *The Journal of Bone and Joint Surgery* 54-A:511–533, 1972

[18] Miller, J. A. A. – Schultz, A. B. – Warwick, D. N. – Spencer, D. L. (1986): Mechanical properties of lumbar spine motion segments under large loads. *Journal of Biomechanics* 19 (1), 79-84. https://doi.org/10.1016/0021-9290(86)90111-9

[20] Natarajan, R. N. – Andersson, G. B. (1999): The influence of lumbar disc height and cross-sectional area on the mechanical response of the disc to physiologic loading. *Spine* 1999; 24:1873–81.

[21] Rohlmann, A. – Zander, T. – Schmidt, H. – Wilke, H-J. – Bergmann, G. (2006): Analysis of the influence of disc degeneration on the mechanical behavior of a lumbar motion segment using the finite element method. *Journal of Biomechanics* 39:2484–2490. https://doi.org/10.1016/j.jbiomech.2005.07.026

[22] Bendoukha, M. – Mosbah, M. (2017): Biomechanical Evaluation of Lumbosacral Segments Response under Physiological Functions: Finite Element Analysis. *Építőanyag – Journal of Silicate Based and Composite Materials*, Vol. 69, No. 4 (2017), 122–126. p. https://doi.org/10.14382/epitoanyag-jsbcm.2017.21

[23] Illien-Jünger, S. – Walter, B. A. – Mayer, J. E. – Hecht, A. C. – Iatridis, J. C. (2014): Intervertebral Disc Culture Models and Their Applications to Study Pathogenesis and Repair. In: Shapiro I., Risbud M. (eds) *The Intervertebral Disc. Springer, Vienna* https://doi.org/10.1007/978-3-7091-1535-0_22

Ref.:

Mosbah, Moustafa – **Bendoukha**, Mohammed: *Anisotropic response of the Holzapfel's constitutive model for the lumbar spine considering degenerative conditions*

Építőanyag – Journal of Silicate Based and Composite Materials, Vol. 70, No. 4 (2018), 110–114. p. https://doi.org/10.14382/epitoanyag-jsbcm.2018.20

The ICCC 2019 will present cement and environmental development worldwide and renowned experts from all over the world are invited to present their work at the Congress. The scientific programme will cover the topics of the newest and the most important research and development describing cement and clinker chemistry (incl. kiln process technology), the nano and macro properties of the clinker and cement, hydration processes, the impact of additives and admixtures, leaching processes, the behaviour of trace elements, microscopy outputs, alternative binders, durability of concrete, standards and codes, as well as modern laboratory instrument equipment. The Congress will consist of many plenary lectures and parallel sessions on a variety of topics, offering to the scientists, researchers, producers and users from all over the world the opportunity to meet, to present and to exchange their research results and knowledge.

September 16–20, 2019

www.iccc2019.org

Preparation of new nano-organoclays from Hexadecylamine, Tetradecylamine and Chalcone with Montmorillonite using ion exchange processes

Manar Ghyath ABD-ALMUTALIB AL-MOSAWY ▪ Department of Chemistry, Faculty of Science, University of Kufa

Emad Abbas Jaffar AL-MULLA ▪ College of Health and Medical Techniques, Al-Furat Al-Awsat Technical University ▪ almullaemad@gmail.com

Érkezett: 2018. 04. 08. ▪ Received: 08. 04. 2018. ▪ https://doi.org/10.14382/epitoanyag-jsbcm.2018.21

Abstract

This study reports the effect of three new organic cations including hexadecylamine (HDA), tetradecylamine (TDA) and 1-(4-aminophenyl)-3-(4-chlorophenyl)prop-2-en-1-one, chalcone (CH) on the basal spacing of the montmorillonite clay to MMT modification. Fourier Transform infrared spectroscopy (FTIR) was used to evaluate the incorporation of these cations in the MMT. X-ray diffraction technique was utilized to indicate the basal spacing of the treated clay as a measure of susceptibility of new organoclays. The FTIR and XRD results shown that the three new organic cations were successfully incorporated in the montmorillonite clay.

Keywords: sodium montmorillonite, modification, surfactant, organic cation

Kulcsszavak: nátrium montmorillonit, modifikálás, felületaktív anyag, szerves kation

Manar Ghyath ABD-ALMUTALIB AL-MOSAWY is a PhD student at Department of Chemistry, Faculty of Science, University of Kufa, Iraq; She has received her MSc from Faculty of Education for Girls, University of Kufa, Iraq in 2010. Main fields of interest: organic synthesis, nanomaterials, biopolymer nano-composites. She has published many scientific papers in citation and non-citation indexed journals .

Emad Abbas Jaffar AL-MULLA is an Asst. Prof., College of Health and Medical Techniques, Al-Furat Al-Awsat Technical University, Iraq; He has received his PhD from University Putra Malaysia, Malaysia in 2010, He was a Post Doctoral researcher at the same University from April 2012 to April 2013; main fields of interest: bioorganic synthesis, nanomaterials, biopolymer nano-composites; He has more than 50 papers in Scopus and ISI journals; his H-Index = 14 according to Scopus database.

1. Introduction

Sodium montmorillonite (MMT) is a naturally occurring clay mineral characterized by relatively low negative charge of its aluminosilicate layers as a result of octahedral substitutions of Al by Mg (II), Fe (II) or other divalent metal ions in a central octahedral sheet (Meleshyn, Bunnenberg, 2006). This negative charge is compensated by inorganic cations such as Na^+, K^+, $Ca^{2+}$and Mg^{2+} in the interlayer space while these inorganic cations can be exchanged by other cations (Chen *et al.*, 2008). However, cation-exchange reaction have been traditionally exploited as an effective method to replace these inorganic ions with organic cationic surfactant molecules, which intercalate into the clay gallery, resulting in expansion of the interlayer spacing and leading to an increase in the basal spacing. These organic cations render the surface of the clay mineral hydrophobic, leading to the increase of the clay wettability and providing favourable interactions with organic molecules. Both organic-modified and unmodified clays have been used for different industrial applications such as rheological additives, thickeners in coating products glues, plastisols, drilling fluids and cosmetics (Jaynes, Boyd, 1991). Recently, clays were used in the field of materials science such as solid phase polymeric nanocomposites. In the 1990's, the use of organically modified clays in polymer-clay nanocomposites has attracted researchers into this area of materials science and technology (Zhang, Wilkie, 2003). The organic modification of clay minerals leads to a decrease in surface energy making clays compatible with polymers. The surface energy of clay minerals and polymer can be determined from contact angle measurements (Maiti, Bhowmick, 2005; Stretz *et al.*, 2005). Studies reported that melt processed nylon 6-clay nanocomposites was prepared using organoclay. Based on X-ray diffraction analysis, various arrangement of alkyl chains in organoclays HDA proposed by Lagaly (1986). Novel organo-montmorillonites have been synthesized and characterized using different ammonium compounds (Rajkrian *et al.*, 2008; Arroyo *et al.*, 2003). Series of anion-cation surfactants modified organoclays were prepared by incorporating of cationic surfactant hexadecyltrimethyl ammonium bromide and anionic surfactant, sodium dodecylsulfonate to montmorillonite (Chen *et al.*, 2008; Rathanawan *et al.*, 2001). In this study, three different ammonium; HDA, TDA and CH were used to modify the compatibility of montmorillonite clay with polymer. These organo-montmorillonites can be used in both medical and industrial applications as polymer nanocomposite.

2. Experimental

2.1. Materials

Sodium montmorillonite, Hexadecylamine and Tetradecylamine obtained from Sigma Aldrich, Germany were used. Hydrochloric acid was obtained from J.T. Baker, USA. p-aminoacetophenone and p-chlorobenzaldehyde were obtained from Fluka. Sodium hydroxide was obtained from B.D.H.

2.2. Preparation of CH (Sadiq *et al.*, 2015)

0.5 g (1 mmol) of p-aminoacetophenone with 1 mmol p-chlorobenzaldehyde were mixed, then 0.5 mL of 10% NaOH aqueous solution and 5 mL of 99% ethanol were added to the mixture. The mixture was stirred at room temperature for 4 hrs. The crude mixture was poured in to ice water and then

acidified the product with 10% HCl solution. The solid formed was filtered then washed with ethanol and water at a ratio of 10:5 mL. Recrystallization from 99% ethanol afforded (67% yield, yellow solid, m.p 160–165 °C).

2.3. Preparation of organoclays (OMMTs)

Organoclay was prepared with a cationic exchange process, where Na in the MMT was exchanged with the alkylammonium ion, which was prepared applying the procedure reported by Al-Mulla *et al.* (2011) in an aqueous solution. Sodium montmorillonite (Na-MMT) 4.00 g was stirred vigorously in 600 mL of hot distilled water for 1 h to form a clay suspension. 4.50 g of HDA, TDA and CH, which HDA been dissolved separately in 400 mL of hot water with 16.00 mL of concentrated hydrochloric acid were added into the clay suspension. After being stirred vigorously for 1 h at 80 °C, the organoclay suspension was filtered and washed with distilled water until no chloride was detected with a 1.0 M silver nitrate solution. It was then dried at 60 °C for 72 h. The dried organoclay was ground until the particle size was 100μm (Al-Mulla *et al.*, 2010a; 2010b). Structure of HDA, TDA and CH is shown in *Fig. 1.*

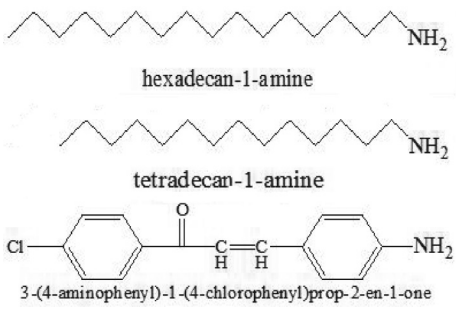

Fig. 1. Structures of the three organic cations
1. ábra A három szerves kation szerkezete

2.4. Characterization

Organoclays were characterized using two different techniques including X-ray diffraction and Fourier Transform Infrared Spectroscopy.

2.4.1. X-ray diffraction (XRD) analysis

X-ray diffraction (XRD) study was carried out using a Shimadzu XRD 6000 diffractometer with Cu K radiation (k = 0.15406 nm). The diffractogram was scanned in the ranges from 2° to 10° at a scan rate of 1°/min.

2.4.2. Fourier Transform Infrared (FTIR) spectroscopy

The FTIR spectra of the blend samples were recorded by the FTIR spectrophotometer (Perkin Elmer FT-IR-Spectrum BX, USA) using KBr disc technique.

3. Results and discussion

3.1. XRD analysis

The alkyl ammonium cation exchange enable the conversion of the hydrophilic interior clay surface into the hydrophobic surface and consequently increase the layer distance as well (Phua *et al.*, 2013). Na-MMT was surface treated with HDA, TDA and CH as intercalation agents through cation exchange process. The cationic head groups of the intercalation agent molecule would preferentially reside at the layer surface and the tail of the compound will radiate away from the surface. The presence of these chains in the galleries makes the originally hydrophilic silicate to organophilic and thus, increase the layer-to-layer spacing of Na-MMT (Al-Mulla *et al.*, 2009). The obtained HDA-MMT, TDA-MMT and CH-MMT were studied using XRD measurements in the 2Θ ranges from 2° to 10°. Na-MMT shows a d001 diffraction peak at 2Θ = 6.91° which, assigns to the interlayer distance of the natural montmorillonite with a basal spacing of 1.27 nm (Agag, Takeichi, 2001). *Fig. 2* reveals XRD the basal spacing (d001 value) increase from 1.27, 1.51, 1.57 and 1.78 nm for Na-MMT, HDA-MMT, TDA-MMT and CH –MMT, respectively.

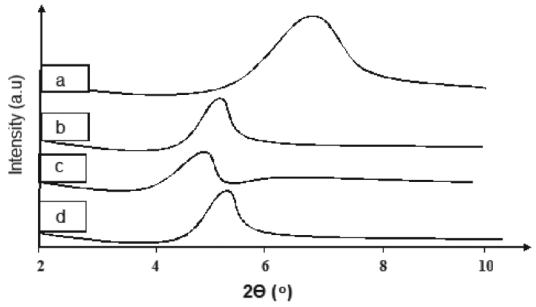

Fig. 2. The XRD patterns of (a) Na-MMT, (b) HDA-MMT, (c) TDA-MMT and (d) CH-MMT
2. ábra Röntgendiffraktogramok; (a) Na-MMT, (b) HDA-MMT, (c) TDA-MMT **és** *(d) CH-MMT*

HDA, TDA, CH have been incorporated into the Na-MMT galleries to products organoclays. The basal spacings and angles of these organoclays were shown Table 1. Thus, XRD result indicate that organoclays are successfully intercalated into the silicate layer.

Sample	Exchanged cation	2Θ (°)	d(001) spacing (nm)
Montmorillonite	Na^+	6.91	1.27
HDA	$C_{16}H_{32}NH_3^+$ (HDA^+)	5.64	1.57
TDA	$C_{14}H_{28}NH_3^+$ (TDA^+)	4.96	1.78
CH	$C_{15}H_9ClO\ NH_3^+$ (CH^+)	5.86	1.51

Table 1. Diffraction angle and basal spacing of montmorillonite and modified montmorillonite with different organic cations
1. táblázat Diffrakciós szög és rácssík távolság; montmorillonit és különböző szerves kationokkal modifikált montmorillonit

3.2. FTIR spectroscopy

FTIR spectra are a useful technique to verify the presence of HDA^+, TDA^+ and CH^+ in the clay. *Fig. 3* shows the FTIR spectra of Na-MMT, pure HDA and HDA-MMT, *Fig. 4* shows the FTIR spectra of Na-MMT, pure TDA and TDA-MMT, *Fig. 5* shows the FTIR spectra of Na-MMT, pure CH and CH-MMT. The infrared spectrum of the Na-MMT shows two peaks, which correspond to Si-O stretching at 1033 cm^{-1} and interlayer water deformation vibration at 1632 cm^{-1} (Guo *et al.*, 2006). The band at 3625 cm^{-1} results from the O-H

stretching vibration and the band at 3043 cm^{-1} results from the CH= stretching vibration back to compound CH. The peaks observed at 2924-2854 cm^{-1}, 2926-2852 cm^{-1} and 2850-2920 cm^{-1} correspond to the presence of the C-H asymmetric and symmetric stretching vibration for HDA-MMT, TDA-MMT and CH-MMT, respectively. The IR spectrum reveals a weak incorporate of the compound CH in the clay (*Fig. 5.c*).

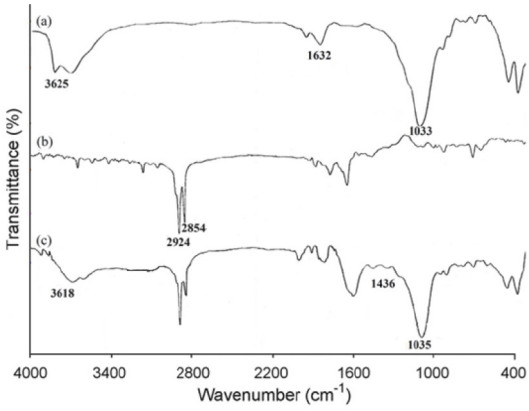

Fig. 3. FTIR spectra of (a) Na-MMT, (b) pure HDA and (c) HDA-MMT
3. ábra FTIR spektrumok; (a) Na-MMT, (b) tiszta HDA és (c) HDA-MMT

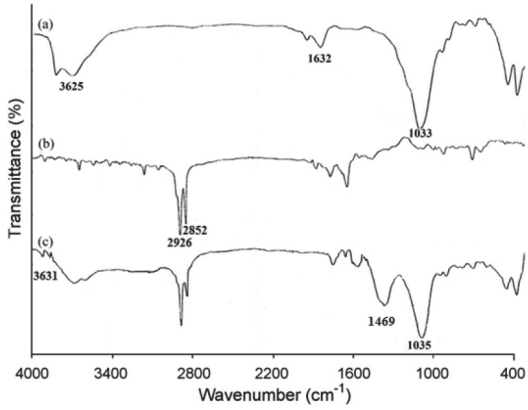

Fig. 4. FTIR spectra of (a) Na-MMT, (b) pure TDA and (c) TDA-MMT
4. ábra FTIR spektrumok; (a) Na-MMT, (b) tiszta TDA és (c) TDA-MMT

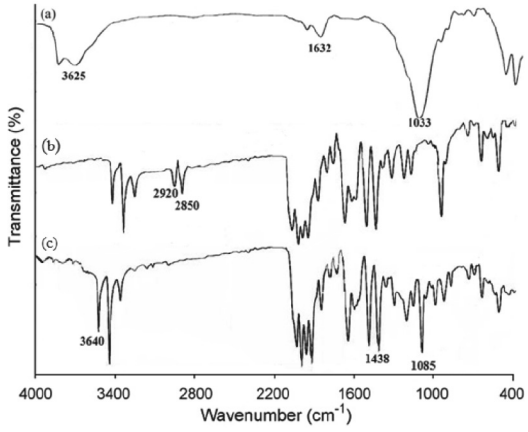

Fig. 5. FTIR spectra of (a) Na-MMT, (b) pure CH and (c) CH-MMT
5. ábra FTIR spektrumok; (a) Na-MMT, (b) tiszta CH és (c) CH-MMT

In the spectra of HDA-MMT, TDA-MMT and CH-MMT, the absorption bands 3618, 3631 and 3640 cm^{-1} indicate the presence of free O-H stretching and at 1035, 1033 and 1085 cm^{-1} correspond to C-N stretching, respectively (Ramachandran *et al.*, 2007). In addition to the bands of the original Na-MMT the band at 1436, 1469 and 1438 cm^{-1} suggest the existence of the ammonium ion. Therefore, these indicate that HDA^+, TDA^+ and CH^+ were intercalated in the silicate layers. This suggests that HDA, TDA and CH are sorbed into the silicate layers of Na-MMT.

4. Conclusions

Three new ammonium cations including HDA, TDA and CH were used to modify montmorillonite clay in an attempt to create susceptible clay to polymers. The organoclays were characterized using FTIR and XRD based on results of this study. Based on results of this study, the following conclusions can be drawn:

- These ammonium cations can be successfully incorporated in the montmorillonite clay.
- The basal spacing of the montmorillonite clay increases as a result of incorporating HDA, TDA and CH.
- The IR spectrum showed that there is a weak incorporate of the compound CH in the clay.
- The new organoclay can be used to produce polymer nanocomposites.

References

[1] Agag, T. – Takeichi, T. (2001): Polybenzoxazine montmorillonite hybrid nanocomposites: synthesis and characterization. *Polymer*. Vol. 41, No. 19, pp. 7083 - 7090. https://doi.org/10.1016/S0032-3861(00)00064-1

[2] Al-Mulla, E. A. J. (2011): Preparation of polylactic acid/epoxidized palm oil/fatty nitrogen compounds modified clay nanocomposites by melt blending. *Polymer Science*, Series A. Vol. 53, pp. 149 - 157. https://doi.org/10.1134/S0965545X11020015

[3] Al-Mulla, E. A. J. – Suhail, A. H. – Saadon, A. A. (2011): New biopolymer nanocomposites based on epoxidized soybean oil plasticized poly(lactic acid)/fatty nitrogen compounds modified clay: Preparation and characterization. *Industrial Crops and Products*. Vol. 33, pp. 23 – 29. https://doi.org/10.1016/j.indcrop.2010.07.022

[4] Al-Mulla, E. A. J. – Mansor, B. A. – Wisam, H. H. – Noor, A. I. (2009): Modification of Montmorillonite by New Surfactants. *Journal of Engineering and Applied Sciences*. Vol. 4, pp. 184 - 188.

[5] Al- Mulla, E. A. J. – Yunus, W. M. Z. – Ibrahim, N. A. – Rahman, M. Z. (2010): Epoxidized Palm Oil Plasticized Polylactic Acid/Fatty Nitrogen Compound Modified Clay Nanocomposites: Preparation and Characterization. *Polymers and Polymer Composites*. Vol. 18, No. 8, pp. 451 – 460.

[6] Al-Mulla, E. A. J. – Yunus, W. M. Z. – Ibrahim, N. A. – Rahman, M. Z. A. (2010): Enzymatic synthesis of fatty amides from palm olein. *Journal of Oleo Sciences*. Vol. 59, No. 2, pp. 157 – 160.

[7] Arroyo, M. – Lopez-Manchado, M. A. – Herrero, B. (2003): Organo-montmorillonite as substitute of carbon black in natural rubber compounds. *Polymer*. Vol. 44, pp. 2447 – 2453. https://doi.org/10.1016/S0032-3861(03)00090-9

[8] Meleshyn, A. – Bunnenberg, C. (2006): Interlayer Expansion and Mechanisms of Anion Sorption of Na-montmorillonite Modified by Cetylpyridinium Chloride: A Monte Carlo Study. *The Journal of Physical Chemistry*. Vol. 110, No. 5, pp. 2271 - 2277. https://doi.org/10.1021/jp056178v

[9] Chen, D. – Zhu, J. X. – Yuan, P. – Yang, S. J. – Chen, T. H. – He, H. P. (2008): Preparation and characterization of anion-cation surfactants modified montmorillonite. *Journal of Thermal Analysis and Calorimetry*. Vol. 94, pp. 841 – 848. https://doi.org/10.1007/s10973-007-8905-y

[10] Guo, L. – Wu, S. – Zeng, F. – Zhao, J. (2006): Synthesis and fluorescence property of terbium complex with novel Schiff-base macromolecular legend. *European Polymer Journal*. Vol. 42, pp. 1670 – 1675. https://doi.org/10.1016/j.eurpolymj.2006.01.025

[11] Jaynes, W. F. – Boyd, S. A. (1991): Clay mineral type and organic compound sorption by hexadecyltrimethylammonium exchanged clays. *Soil Science Society of America Journal*. Vol. 55, pp. 43 - 48.

[12] Maiti, M. – Bhowmick, A. K. (2005): Structure and properties of some novel fluoroelastomer/clay nanocomposites with special reference to their interaction. *Journal of Applied Polymer Science*. Vol. 44, pp. 162 - 176. https://doi.org/10.1002/polb.20680

[13] Rajkiran, R. T. – Kartic, C. K. – Upendra, N. (2008): Synthesis and characterization of novel organo-montmorillonites. *Applied Clay Science*. Vol. 38, pp. 203 - 208. https://doi.org/10.1016/j.clay.2007.05.008

[14] Ramachandran, E. – Baskaran, K. – Natarajan, S. (2007): XRD, thermal, FTIR and SEM studies on gel grown gamma-glycine crystals. *Crystal Research and Technology*. Vol. 42, pp. 73 - 77. https://doi.org/10.1002/crat.200610774

[15] Rathanawan, M. – Wittaya, L. – Anuvat, S. – Johannes, W. S. (2001): Preparation, structure, properties and thermal behavior of rigid-rod polyimide/montmorillonite nanocomposites. *Composites Science and Technology*. Vol. 61, pp. 1253 – 1264. https://doi.org/10.1016/S0266-3538(01)00026-4

[16] Sadiq, S. A. – Atiyah, E. M. – Numan, A. T. – Sanak, K. A. (2015): Synthesis and characterization of new bidentate chalcone ligand type (NO) and its Mn^{II}, Co^{II}, Ni^{II} and Cu^{II} complexes with study of their antibacterial activity. *Diyala Journal For Pure Sciences*. Vol. 11, No. 3, pp. 2222-8373.

[17] Stretz, H. A. – Paul, D. R. – Lib, R. – Keskkula, H. – Cassidy, P. E. (2005): Intercalation and exfoliation relationships in melt-processed poly(styrene-co-acrylonitrile)/montmorillonite nanocomposites. *Polymer*. Vol. 46, pp. 2621 - 2637. https://doi.org/10.1016/j.polymer.2005.01.063

[18] Phua, Y. J. – Chow, W. S. – Ishak, Z. A. M. (2013): Organomodification of montmorillonite and its effects on the properties of poly(butylene succinate) nanocomposites. *Polymer Engineering & Science*. Vol. 53, pp. 1947 - 1957. https://doi.org/10.1002/pen.23460

[19] Zhang, J. – Wilkie, C. A. (2003): Preparation and flammability properties of polyethylene-clay nanocomposites. *Polymer Degradation and Stability*. Vol. 80, pp. 163 - 169. https://doi.org/10.1016/S0141-3910(02)00398-1

Ref.:
Abd-Almutalib Al-Mosawy, Manar Ghyath – **Al-Mulla,** Emad Abbas Jaffar: *Preparation of new nanoorganoclays from Hexadecylamine, Tetradecylamine and Chalcone with Montmorillonite using ion exchange processes*
Építőanyag – Journal of Silicate Based and Composite Materials, Vol. 70, No. 4 (2018), 116–119. p.
https://doi.org/10.14382/epitoanyag-jsbcm.2018.21

Mass transfer of aluminum film from the surface of zeolite on the cathode

N. N. LEBEDEVA ▪ Institute for Problems, Baku State University ▪ nnlebedeva@gmail.com
V. I. ORBUKH ▪ Institute for Problems, Baku State University ▪ orbukh@ramblero.ru
G. M. EYVAZOVA ▪ Institute for Problems, Baku State University ▪ eygoncha@mail.com
N. H. DARVISHOV ▪ Institute for Problems, Baku State University ▪ n_darvishov@mail.ru
Ch. G. AKHUNDOV ▪ Institute for Problems, Baku State University ▪ ch.axundov@mail.ru
Érkezett: 2018. 04. 17. ▪ Received: 17. 04. 2018. ▪ https://doi.org/10.14382/epitoanyag-jsbcm.2018.22

Abstract
In the present study, the phenomenon of mass transfer of an aluminum film deposited on the zeolite surface onto a clamping electrode was observed. The proposed four-layer model explains the very fact of mass transfer (inhomogeneous over the cross section of the structure) in the absence of anomalously large electric fields at the cathode.
Keywords: zeolite, mass transfer, clinoptilolite, zeolite pores, zeolite framework
Kulcsszavak: zeolit, tömegáram, klinoptilolit, zeolit pórusok, zeolit vázszerkezet

Nelli N. LEBEDEVA
Graduated at Baku State University in 1960 with a specialty in Physics of Semiconductors and Dielectrics. Field of interests: physical phenomena inhomogeneous system 1) ferroelectrics-semiconductor; 2) photoconductors-plasma of a gas discharge; 3) dielectrics (zeolites) -conductors (graphite, silicon, Ag, Cu)

Vladimir I. ORBUKH
Graduated at Baku State University in 1971 with a specialty in Physics of Semiconductors and Dielectrics. Field of interests: theory of physical phenomena inhomogeneous system 1) ferroelectrics-semiconductor; 2) photoconductors- plasma of a gas discharge; 3) dielectrics (zeolites) –conductors (graphite, silicon, Ag, Cu)

Goncha M. EYVAZOVA
Graduated at Baku State University (BSU) department of Physics in 1974. Completed her PhD degree under the supervision of Prof. A. M. Mamedov at BSU. Now she is leading scientific researcher in Nano Center, Department of Physics, BSU. Her current research interests include the synthesis of nanostructured metal chalcogenides, various nanoparticles, and investigation of optical and electrical properties.

Namiq H. DARVISHOV
Graduated at Baku State University in 1974 with a specialty in Physics of Semiconductors and Dielectrics. Field of interests: 1) optical; 2) ferroelectrics-semiconductor; 3) photoconductors-plasma

Chingiz G. AKHUNDOV
Graduated at Baku State University in 1976 with a specialty in Physics of Semiconductors and Dielectrics. Field of interests: physical phenomena inhomogeneous system 1) ferroelectrics-semiconductor; 2) photoconductors-plasma of a gas discharge; 3) dielectrics (zeolites) -conductors (graphite, silicon, Ag, Cu)

1. Introduction

Zeolites are aqueous aluminosilicates,the infinite aluminosilicate frame of which is formed by the joint of the common vertices of $[SiO_4]^4$ and $[AlO_4]^5$ tetrahedra, having interconnected cavities occupied by large ions and water molecules [1]. The loosely bound cations and water molecules in the pores of the zeolites are characterized by considerable mobility, which allows ion exchange and reversibility of the dehydration without affecting the aluminosilicate rigid framework. Due to this property zeolites have extremely wide scope of use in industry and agriculture.

Currently, more than 45 types of natural zeolites are known, of which the most common are clinoptilolite, heylandite, phillipsite, lomonite, mordenite, erionite, chabazite, ferrierite, analcime. Clinoptilolite is defined as a series of zeolitic minerals having a clear structural topology of heylandite (HEU) and a Si/Al ratio of 4.0.

The structural topology of the tetrahedral HEU lattice has been extensively studied and has a C2/m symmetry with oblate channels bounded by ten-membered channels (7.5×3.1A) and eight-membered tetrahedral rings (4.6×3.6 A) parallel to the C axis. The additional eight-membered circular channels (4.7×2.8 A) are parallel [100] and [102] and intersect with the preceding channels within [010], forming a system of two-dimensional parallel channels to [010], which are responsible for the layered structure [1, 2].

Analysis of data on the structure and properties allows us to consider this zeolite not only as a promising sorbent, but also as an object on which it is possible to investigate poroemission of electrons, electron multiplication and gas discharge in pores [3], dielectric and electrical properties [4]. If the sorption properties of the zeolite are determined by the size and configuration of the pores, then its electrical properties are determined by the composition of the substance in the pore space [5]. On the basis of X-ray and spectral chemical analysis, we established that the natural zeolite we are studying belongs to high-silica zeolites of the clinoptilolite type [6]. The content of the channels, which is an off-frame subsystem, is positively charged Na +, K +, Mg +, Ca + ions that compensate for the negative charge of the framework, as well as a large number of molecules of H_2O-coordination water.

Water plays an important role in ensuring the stability of the clinoptilolite framework and, as suggested, leads to an increase in the mobility of ions in the pore space. Loosely bound cations and water molecules in pores of zeolites lead to high values of the dielectric constant at low frequencies and a significant dependence of the electrophysical properties of seolites on frequency and temperature. The ability of cations to diffuse through a large open zeolite structure makes it possible to obtain high ionic conductivity in zeolites. In recent years, many attempts have been made to investigate the factors that control ion transport in an external electric field [7]. These

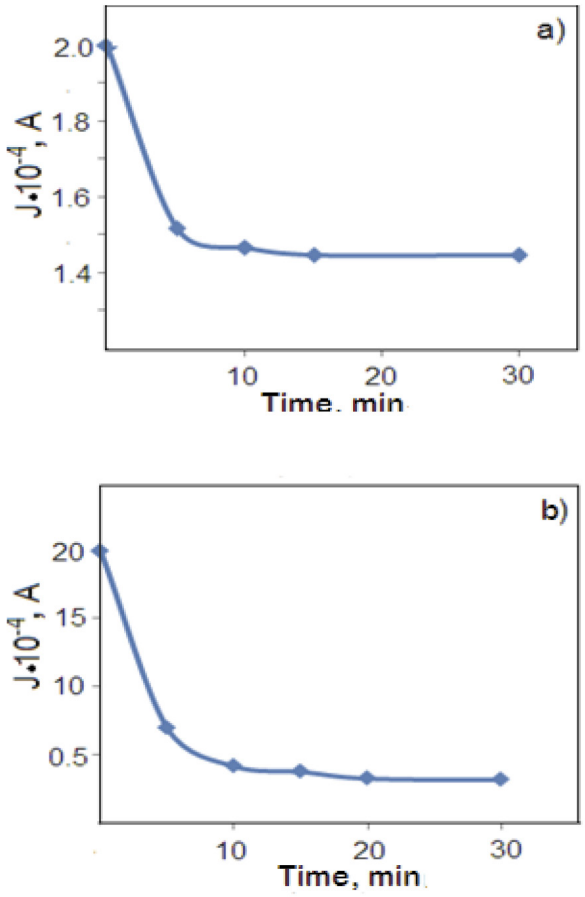

Fig. 1. The time dependence of the current at a negative (a) and a positive (b) electrode potential

1. ábra Áramerősség időfüggése (a) negatív és (b) pozitív elektródpotenciál esetén

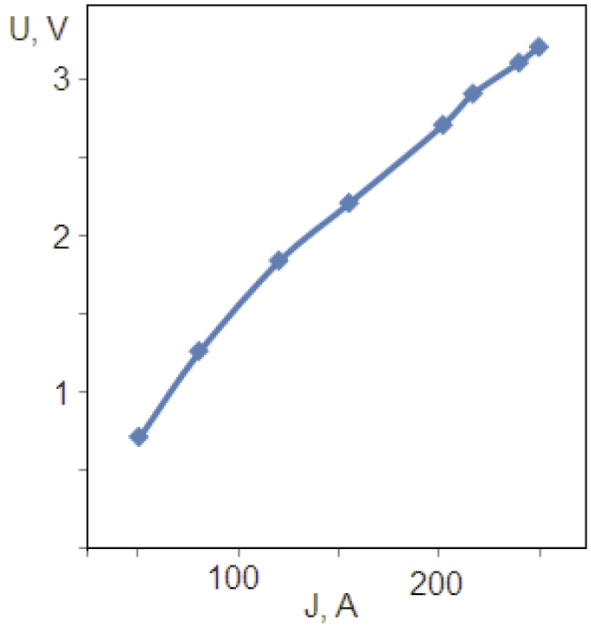

Fig. 2. The current-voltage characteristic of a plate with aluminum sputtered on one side

2. ábra Áramerősség-feszültség karakterisztika egy oldalán alumíniummal bevont lemez esetén

studies are focused mainly on the effect of temperature, the degree of hydration, the nature of the metallic cations on the conductivity, measured at alternating voltage.

In the present work, a mass transfer of a metal film deposited on the surface of a plate of natural zeolite to a negatively charged electrode is observed when a sufficiently weak constant electric field is applied.

The processes of mass transfer in the electrode-sample contact take place during welding, when the welding current is turned on, as the pre-electrode region of the heating is heated, the plastic deformation resistance decreases, respectively, the actual contact areas expand and the processes of mutual diffusion of metals develop. The mass transfer rate is controlled by the temperature in contact, the residence time of metals at elevated temperatures, the state of the surfaces of parts and electrodes, and the physical properties of the metals to be welded.

Another mechanism of, mass transfer is field desorption and field ionization [8]. The desorption theory and field evaporation consider the case of emission of positive ions in a strong electric field. Theoretical estimates of the desorption intensity for various metals are in the range 1428-288 Mv/sm.

All the above conditions are not implemented in our case.

Materials: The natural zeolite clinoptilolite was used as an object of study: syngonia-monoclinic, space symmetry group C2/m; the unit cell parameters: a = 1.761, b = 1.780, c = 0.741 nm, β = 115.2°. For the experiment from a bulk monoblock of natural zeolite clinoptilolite, the chemical composition of which, confirmed by the X-ray analysis, contained: Al_2O_3 - 11.36, SiO_2 -67.84, Na_2O - 1.25, MgO - 0.49, P_2O_5 - 0.11, SO_3 -0.03, K_2O - 3.01, CaO - 0.29, TiO_2 - 0.08, MnO - 0.078, Fe_2O_3 - 1.19, KJ - 11.64, the plates with the size (15×10×2) 10^{-3} were cut.

Thermal sputtering of aluminum on the ground surface (15×10) of a 10^{-3}sm zeolite plate was carried out in VUP in a vacuum of 10^{-3}torr.

2. Measurements

The plate with aluminum deposited on one side was placed in a cassette, where it was clamped between two polished copper electrodes. The electrodes were supplied with a constant voltage (U = 250V). The time dependence of the current was measured when the electrode pressed to aluminum was a cathode (*Fig. 1.a*) and an anode (*Fig. 1.b*).

In both polarities, the currents slowly decrease with time and after 30 minutes they reach saturation. After achieving a stable current (10^{-4}A), the I-V characteristic was measured (*Fig. 2*).

3. Discussion

It was found that as a result of the current passing through the zeolite plate, the aluminum film on its surface can pass to the electrode. Such an aluminum mass transfer occurs only when the electrode is a cathode. It is important to note that the transfer of aluminum to the clamping electrode is not carried out over the entire area of the film. To explain the observed phenomenon, we will start from the four-layer model: a zeolite plate-an aluminum film on it-a thin air gap-a clamping

electrode. The conductivity of the zeolite is carried out by positive ions moving in the pores of zeolite. In our model, the zeolite ions, moving toward the cathode, fall on the surface of the aluminum film, where they are neutralized due to the metallic conductivity of aluminum. Simultaneously, on the opposite side of the film (from the side of the air gap) the same positive charge arises. In other words, the charge of positive ions of the zeolite that have approached the aluminum film is converted to the same positive charge of aluminum ions on the opposite side of the film. The next stage is the recombination of these positive aluminum ions with electrons from the clamping cathode. This can happen in two ways: either electrons from the clamping electrode will transfer to the surface of the aluminum film, or positive ions of aluminum will transfer to the clamping electrode. The first of these mechanisms is more traditional and is realized when the metal film is a structure close to a single crystal, which provides a high binding energy of the ion with the film. The second mechanism is realized in the case of strongly amorphous films, which are disordered agglomerates with low binding energy of the ion with film. Such films are formed in those cases when the film is deposited on a non-crystalline (and, in general, unordered) surface. In our case, this is exactly the case, as can be seen from *Fig. 3*, which presents a photograph of the surface of the zeolite plate on which aluminum was deposited.

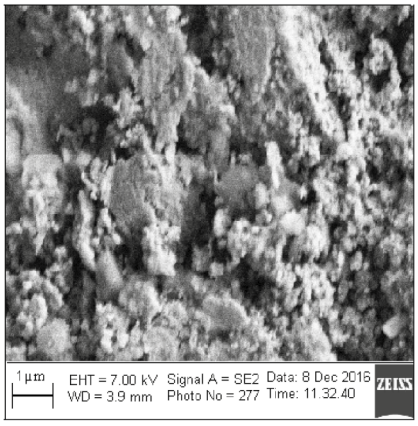

Fig. 3. Morphology of the surface of the zeolite plate
3. ábra Zeolit lemez felületi morfológiája

4. Conclusions

In this paper we show the possibility of mass transfer in the absence of anomalously large electric fields. This is possible due to the large positive charge on the metal amorphous film, which arise, from the neutralization of positive ions of the zeolite.

Acknowledgments

The authors wish to thank Prof. Dr. Amirullah M. Mamedov (Bilkent University) for helpful discussion and reading the manuscript.

References

[1] Gollardi, G. – Galli, E. (1985): Natural Zeolites. *Springer-Verlag*, Berlin, 409 p.
[2] Baerlocher, C. – Meier, W. M. – Oslon, D. H. (2001): Atlas of Zeolite Flamework Types. *Amsterdam*, Elsevier, 302 p.
[3] Lebedeva, N. N. – Orbukh, V. I. – Sultanov, C. A. (2010): Gas-discharge system with a zeolite electrode Technical Physics. Vol. 55, No. 4, pp. 565-568. https://doi.org/10.1134/S1063784210040225
[4] Baryshnikov, S. V. – Lankin, S. V. – Stukova, E. V. – Yurkov, V. V. (2004): Conductivity of ion-replaced forms of clinoptilolite. *Sovremenniye Naukoemkiye Tehnologii*, Vol. 6, pp. 26-27.
[5] Bogomolov, V. N. (1978): Physcs-Uspekhi, (in Russian), Vol. 124, pp. 171.
[6] Kuliyeva, T. Z. – Lebedeva, N. N. – Orbukh, V. I. – Sultanov, Ch. A. (2009): Fizik, (in Russian) Vol. XV, No.3, pp. 43-45.
[7] Kalogeras, J. M. – Vassilikou-Dova, A. (1996): Molecular Mobility in Microporous Architectures: Conductivity and Dielectric Relaxation Phenomena in Natural and Synthetic Zeolites. *Crystal Research & Technology*. Vol.31, No.6, pp. 693-726. https://doi.org/10.1002/crat.2170310602
[8] Muller, E. V. (1987): Auto ionization and auto ionic microscopy, *Physics-Uspekhi*, (in Russian) Vol. LXXVII, c. 3, 1062, pp. 481-551.

Ref.:
Lebedeva, N. N. – **Orbukh**, V. I. – **Eyvazova**, G. M. – **Darvishov**, N. H. – **Akhundov**, Ch.G.: *Mass transfer of aluminum film from the surface of zeolite on the cathode*
Építőanyag – Journal of Silicate Based and Composite Materials, Vol. 70, No. 4 (2018), 120–122. p.
https://doi.org/10.14382/epitoanyag-jsbcm.2018.22

Numerical study of building materials filled by PCM for thermal energy storage

Youcef Oussama SOUCI ▪ Laboratory of Numerical and Experimental Modelling of Mechanical Phenomena, University Abd El Hamid Ibn Badis of Mostaganem, Algeria ▪ souci_youcef@yahoo.fr
Samir HOUAT ▪ Laboratory of Numerical and Experimental Modelling of Mechanical Phenomena, University Abd El Hamid Ibn Badis of Mostaganem, Algeria

Érkezett: 2018. 04. 29. ▪ Received: 29. 04. 2018. ▪ https://doi.org/10.14382/epitoanyag-jsbcm.2018.23

Abstract
Phase change material (PCMs) is used to equilibrate the temperature fluctuation and to store energy in several practical application areas such as electronics, automobile industry and also buildings. In this paper, an example of the application of phase change material in the building application is investigated. The physical problem of phase change is solved by using a numerical study based on the finite element method. The PCM selected in this study, is incorporated directly within the building materials for improving its capacity of thermal storage. Two different building materials are selected according to their usual applying as construction materials for residential buildings. The numerical results have been checked and validated with an experimental model and the error is estimated.
The results reveal the potential of PCM in the enhancement on the thermal inertia of the wall and effectively reduced the fluctuation of the interior surface temperature. In addition, with the increasing filling amount of PCM, the thermal response of the building material will be more effective through improving its thermal insulation and stored more of energy as a latent heat.
Keywords: Building materials, PCM, energy storage, finite element method
Kulcsszavak: Építőanyagok, PCM, energia tárolás, véges elemes eljárás

Youcef Oussama SOUCI
PhD candidate in mechanical engineering under the supervision of Prof. Houat Samir at the laboratory of numerical and experimental modelling of mechanical phenomena. Obtained the licence and Master's degree in civil engineering from the University of sciences end technology of Oran –(USTO) Algeria.

Samir HOUAT
Professor at the University of Mostaganem (UMAB) of Algeria and head of numerical and experimental modelling of mechanical phenomena laboratory. He is the author of several scientific publications. He has been a member of the technical committees on several national and international congress, seminar and journals.

1. Introduction

As demand in thermal comfort of the buildings rises, the energy consumption is correspondingly increasing. For example, in Algeria, the energy consumption of buildings has increased by 22% the last three years. Housing and tertiary buildings are responsible for the consumption of approximately 43% of all energies [1].

At present, the thermal energy storage systems (TESS) are becoming more popular with regard to its incorporation in building materials, which in turn will reduce the dependence on fossil fuels for environmental and economic reasons [2]. The energy content in latent heat allows the PCM to transform its phase (from liquid to solid or vice versa) that permit it to store or release energy according to the required thermal loads [3]. Relying on the phase changing state, we note the three different cases by which the PCMs are characterized (solid-solid / solid-liquid / liquid-gas) [4]. Moreover, the solid-liquid phase changing is most suitable for the storage of thermal energy, where PCMs are clustered in three types: organic, inorganic and eutectic [5-7].

The applications of PCM can be extended to several disciplines such as medicine, sports and construction [8-9]. The integration of PCM in building materials such as concrete, ceramics, glass and hollow brick [10-16] is a way to enhance the storage capacity of building envelope and then to rationalize the use of renewable and non-renewable energies.

These studies have requested an improvement in thermal inertia, in order to store thermal energy [17]. The most effective method is using PCMs in both cooling and passive and active heating of the building.

The ways by which the PCMs are incorporated, namely the direct incorporation, immersion and encapsulation have been analyzed by Hawes and Feldman [18].

Soaresa et al [19], provided a comprehensive review on the previous research addressing the passive latent heat thermal energy storage systems with PCM in buildings and their related performance. The study covers different characteristics, thermal properties, and selection criteria of PCM. The experiments and the numerical modelling of heat transfer with PCM and different dynamic simulations of energy building with PCM are reported. Finally, the life cycle assessments, both environmental and economic, were discussed.

Castell et al [20], experimentally tested the PCM with two types of typical construction material. The study showed that using the PCM reduces the peak temperature by 1°C and the electrical energy consumption by 15%. Alawadhi [21], one of the few researchers who studied numerically the thermal analysis of two-dimensional model of common building bricks with cylindrical holes integrated PCM to reduce the heat flow by storing energy from outdoor space in a hot climate during the day. This energy was retrieved during night time by solidification of PCM. The study focused on investigating different types of PCM at different melting temperatures, different PCM quantities at different brick's spatial locations. The study reported up to 17.55% savings in energy.

Many studies have investigated the use of PCM in buildings and showed that the PCM can remarkably improve the building energy performance. But few studies have examined the comparison between building materials when using PCM and its practical application.

At the present paper, to determine the influence of the use of the thermal energy system in building applications, a numerical study based on the finite element method has been carried out. To reach this objective, two different construction materials which were usually used in Algeria have been selected. The purpose of this study is to evaluate the total energy storage of these two materials, when filled by PCM, by analyzing and comparing their energetic performance.

2. Materials and methods

2.1 Material descriptions

Two building materials filled by PCM are carried out. The first one (M1) is the hollow brick and the second material (M2) is the breeze block as shown in *Fig. 1*. The hollow brick used consisting of 8 internal empty holes which have a parallelepiped section (3.5 × 3.5 cm²). The total dimensions of this material are thickness = 10 cm, width = 20 cm and length 30 cm. For the breeze block is consists of 6 parallelepiped holes (7 × 14 cm²) and its total dimensions are thickness = 20 cm, width = 50 cm and length = 20 cm.

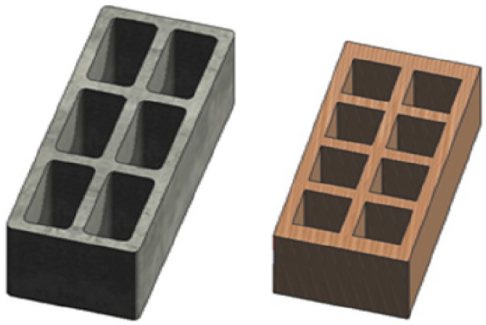

Fig. 1. Left: Hollow brick; Right: Breeze block
1. ábra Bal: üreges tégla, jobb: falazóblokk

The PCM selected and used in the present work is the organic paraffin n-octadecane with a phase change temperature of PCM at the main peak is 27.6 °C and the latent heat is about 243.5 kJ/kg [17]. This PCM was chosen because of its compatibility with closed container made of plastic in order to prevent its leakage at the liquid state and also because they are considered non corrosive and are chemically inert. The thermo physical characteristics of hollow brick, breeze block and PCM are shown in *Table 1*.

Material	Density (kg/m³)	Thermal Conductivity (W/m·K)	Heat capacity (J/kg·K)
PCM (solid)	865	0.358	1934
PCM (liquid)	780	0.148	2196
Hollow Brick	1600	0.7	840
Breeze Block	1300	1.05	648

Table 1. Characteristics of PCM and building materials used
1. táblázat PCM és falazóblokkok jellemzői

2.2 Governing equations and boundary conditions

In order to simplify the mathematical model, many assumptions are made in this numerical analysis:

- Heat transfer process across the building material with PCM is unsteady and is treated as a one-dimensional problem (because these building material represent elements of a wall which its thickness is smaller than the other dimensions).
- The PCM material used is pure, homogeneous and isotropic.
- All thermo-physical properties of the building materials were kept constant except the conductivity and specific heat of PCM may be different in the liquid and solid phases.
- The natural convection of the PCM during the melting process and the super-cooling effect during the freezing process can be neglected when the temperature difference between the initial conditions and boundary is small [22].
- The interface layers between the building material and the PCM are homogeneous with perfect contact between them, which means that contact resistance is neglected.
- The surrounding radiation is neglected.

The transient enthalpy equation is given by Eq. (1):

$$\rho \frac{\partial h}{\partial t} = \lambda \frac{\partial^2 T}{\partial x^2} \tag{1}$$

For the Non-PCM layer, the enthalpy (KJ/kg) is given only by the sensible enthalpy as shown in Eq. (2) and for The PCM layer, the enthalpy (KJ/kg) is computed in Eq. (3) as the sum of the sensible enthalpy and the latent heat.

$$h = h_{ref} + \int_{T_{ref}}^{T} C_p \, \partial T \tag{2}$$

$$h = h_{ref} + \int_{T_{ref}}^{T} C_p \, \partial T + fL \tag{3}$$

Where h_{ref} is the reference enthalpy at the reference temperature T_{ref}, f is the liquid fraction and L is the latent heat of PCM (KJ/kg). The liquid fraction of PCM is defined as:

$$f = \begin{cases} 0, & if \;\; T < T_m \quad (solid) \\ 1, & if \;\; T > T_m \quad (liquid) \end{cases} \tag{4}$$

Where T_m is the melting temperature of PCM.

For both building materials with and without PCM, Eq. (5) is used to calculate the energy stored by unit of surface *E(t)*:

$$E(t) = \int_0^t (\varphi_{in,s} - \varphi_{ext,s}) dt \tag{5}$$

$\varphi_{in,s}$, $\varphi_{ext,s}$ are the inside and the outside surface heat flux, respectively.

The boundary condition at the indoor and the outdoor surfaces:

$$-\lambda_b \frac{\partial T_b}{\partial x} = h_{c,j}(T_j - T_{j,s}) \tag{6}$$

$$\begin{cases} h_{c,j} = h_{c,in}\,, \;\; T_j = T_{in}\,, \;\; T_{j,s} = T_{in,s} & ; x = 0 \\ h_{c,j} = h_{c,ext}\,, \;\; T_j = T_{ext}\,, \;\; T_{j,s} = T_{ext,s} & ; x = w \end{cases}$$

The numerical values of the convective heat transfer coefficient can be assumed as in [23] $h_{c,ext}$ = 20 W/m² °C and $h_{c,in}$ = 10 W/m² °C.

At the building material/PCM interfaces:

$$\lambda_{pcm}\frac{\partial T_{pcm}}{\partial n} = -\lambda_b\frac{\partial T_b}{\partial n} \quad (7)$$

Where n is the coordinate normal to the surface of the PCM cavity.

3. Numerical validation

Before exhibiting the obtained results, the numerical code is validated by comparison with an experimental solution available in the literature [24]. The experimental setup depends on testing a hollow slab incorporated by PCM. The PCM selected is characterized by a melting temperature equal to 27 °C. At the bottom surface of the slab, a linear increasing is imposed in temperature of 20 °C to 35 °C for one hour (Rate of rise = 1.25 °C/h) and then maintains the temperature at 35 °C for 6 hours. Their top surface is in direct contact with the atmosphere of the laboratory room T_{in} = 0 °C.

A study on mesh type and size has been carried out for this validation. It has been selected a triangular mesh with an element number equal to 2428 and the convergence criterion for temperature used is 10^{-4}.

Fig. 2 shows the comparison between our numerical results with the results that were obtained in the experimental on the variation in the temperature of the bottom and top surfaces of the slabs. For the validation study, the Maximum Error calculated by Eq. (8) is used to assess the difference between experimental and numerical results.

$$\text{Maximum Error (\%)} = \max_{1.2..n}\left\{\left|\frac{T_{exp}-T_{num}}{T_{exp}}\times 100\right|\right\} \quad (8)$$

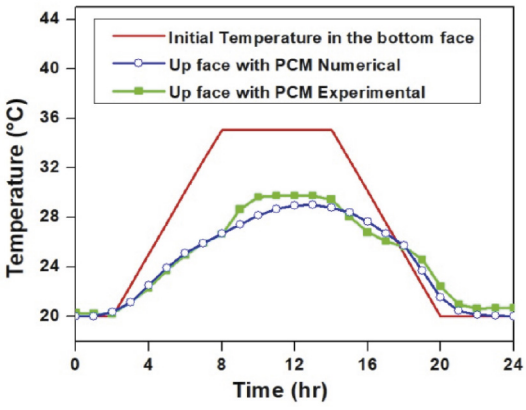

Fig. 2. Temperature at the interfaces of the floor panel
2. ábra Hőmérséklet a födémpanel felületén

As shown in *Fig. 2*, the numerical result agrees well with the experimental measurements with the maximum error of (5%). Three reasons can explain the slight discrepancy between simulation and experimental data. Firstly, the quality of the insulation material that has been used in the experiment to isolate the lateral faces of the slab is not perfect to provide the same performance as that used in the numerical simulation. Secondly, in the experimental study, it has been found that the melting temperature is not equal to the solidification temperature of the PCM. Thus, in the numerical study, this difference between both temperatures could create a sort of imprecision in the selection of the δT value (phase transition zone). Finally, the possibility that the effect of the natural convection in the experimental case is not neglected and it can be integrated into the liquid state of the PCM what is different from the hypotheses that have been taken in the simulation model.

4. Results and discussion

The test results about the influence of the PCM on the thermal storage capacity of two different building materials have been summarized in *Figs. 3* to *5*.

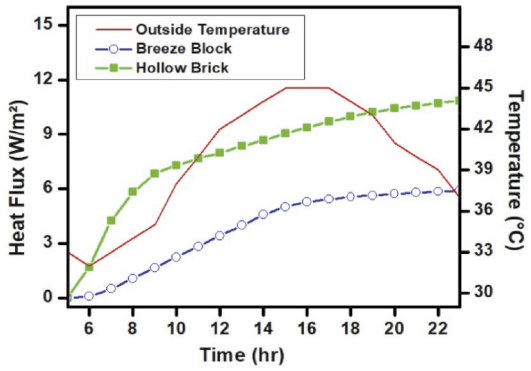

Fig. 3. Heat flux at the indoor surface for both materials with PCM
3. ábra Hőáram mindkét PCM anyaggal kitöltött blokk esetén beltéri felületen

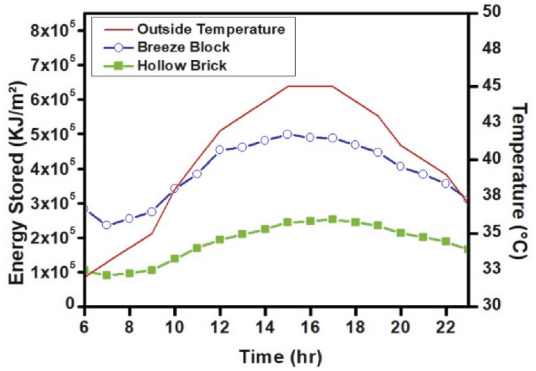

Fig. 4. Energy stored per unit of surface as a function of time
4. ábra Felületre vonatkoztatott hőtárolás az idő függvényében

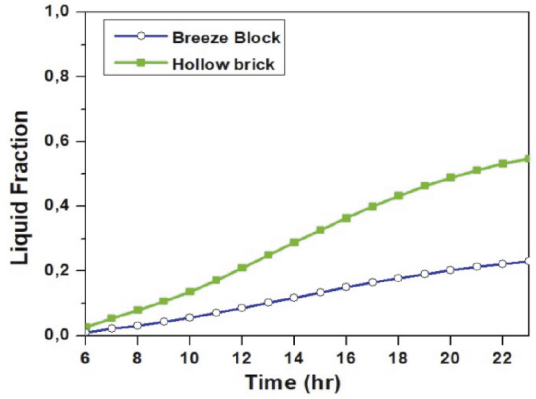

Fig. 5. Liquid Fraction for both materials with PCM
5. ábra Folyadék fázis mindkét PCM anyaggal kitöltött blokkra vonatkozóan

The finite element method is utilized to solve the physical problem. For both building materials selected, it has been used a Free quadrilateral element to mesh the computational domain. The software used at this numerical study offers the possibility to configure an automatic mesh with different element sizes. The choice of the type of mesh is based on the study of the influence of the number of elements on two physical parameters namely the average temperature of model and the liquid fraction of PCM. The results of this study are shown in *Table 2*.

	Number of elements		Temperature (°C)		Liquid Fraction	
Material	Breeze Block	Hollow brick	Breeze Block	Hollow brick	Breeze Block	Hollow brick
Mesh size						
Fine	305	160	27.78	29.09	0.232	0.549
Intermediate	1000	276	27.79	29.06	0.229	0.547
Extremely fine	6976	1375	27.79	29.03	0.228	0.543

Table 2. Effect of the mesh size on the temperature and the liquid fraction of PCM
2. táblázat Hálóméret hatása a hőmérsékletre és a PCM folyadék fázisára

The observation of the results shows the independence of the number of meshes on the values of the temperature and the liquid fraction of PCM. Similarly, beyond a finer mesh, the increase in the number of elements becomes insensitive and it will not necessarily change the solution but it requires a longer calculation time. Therefore, after various mesh tests, it has adopted a Structured quadrilateral mesh with an element number equal to 800 for the hollow brick and 1000 element number for the breeze block.

The two materials selected subject to an external air temperature of a day time as an example of real conditions. Constant temperature is applied as the indoor air temperature T_{in} = 25 °C.

As it is shown in *Fig. 3*, a comparison of the heat flux at the indoor surface between the two building materials is investigated. In the light of the results shown in this figure, the level of the heat flux obtained by the hollow brick is higher than that obtained with the breeze block. One of the significant reasons that lead to this result can be the difference between the PCM amounts inserted within both materials. The amount of PCM in the breeze block is about 83% larger than that used in the hollow brick due to the different geometries between the two materials. Therefore, the hollow brick-PCM system will not benefit a lot from its high latent heat because when a small quantity of PCM is used, this will leads to accelerate the melting/freezing process and making PCM most time in a deactivated mode. On the other hand, for the breeze block with PCM, most of heat will be stored as latent heat rather than as sensible heat due to the large energy needed by PCM in order to complete its phase change process. As a result, more energy will be absorbed by the material instead of being transmitted to the inner side.

Fig. 4 presents the quantity of heat per surface unit as a function of time, which is calculated by using Eq. (5). It can be seen that the thermal energy stored in the breeze block with PCM is larger than that stored in the hollow brick.

At the end of the day, it has been found that the energy stored as latent heat by the PCM placed inside the breeze block is about 2.29×10^6 KJ/m². While, for the PCM inside the hollow brick, it has stored a small quantity of latent heat which is around 10^6 KJ/m².

This result is compatible with what has been mentioned above. As it is observed from the obtained values that as the amount of PCM increases, the demand to store more latent heat becomes important in order to complete the phase change process.

To aid in understanding these results in *Fig. 4*, it has been evaluated the liquid fraction as is shown in *Fig. 5*. It can be seen that more than 50% of the PCM inserted in the hollow brick has converted to the liquid state. In turn, only 25% of the PCM in the breeze block has changed its phase. This finding reveals that most of the energy is stored as a sensible heat in the breeze block with PCM due to the large amount of PCM that has been remained most of the time at its solid state. Thus, it has the opportunity to store more of latent heat and this leads to reduce the heat gain. Due to this fact, using a building material which is capable to contain a larger amount of PCM is more effective to weak the effect of outdoor temperature fluctuation on indoor thermal environment and that by enhancing its thermal insulation effect.

5. Conclusions

A numerical model was established to evaluate the potential of the thermal energy stored when it's applied in the building application. The proposed solution to achieve this is the incorporation of a phase change material in the construction elements. The numerical code is validated with an experimental model in the literature. It has been seen that the numerical results agreed well with the experimental results. Two different building materials are selected as an example to test its capacity of stored energy as a latent heat. Comparing the results from both materials, it is observed that the PCM addition, produces a reduction in the fluctuation of the heat flux at the inner surface of the breeze block more than the hollow brick. It has been explaining this result from the fact that there is a direct correlation between the increases in the amount of PCM and reduced heat flux at the inner surface.

It is observed that for the same test conditions, the breeze block with PCM stores 2 times more energy as a latent heat per unit surface than the hollow brick. This difference is due to the ability of PCM to complete its phase change rapidly. However, using a great quantity of PCM leads to delay the melt/solidification process so that the PCM could benefit more broadly from its potential to store the latent heat. Therefore, in practice and under similar conditions of this study, it is recommended to select a building material that can receive as much PCM as possible. This is because the increasing of the PCM amount has a positive effect on improving the thermal inertia of the building material.

Nomenclature

C_p : Specific heat capacity (kJ/kg·°C)
f : Liquid fraction
h : Enthalpy (kJ/kg)
h_c : Convective heat transfer coefficient
L : Latent heat of fusion, (kJ/kg)
Q_s : Solar flux radiation (W/m²)
T : Temperature (°C)
t : Time (h)
w : Thickness of wall (m)

Greek symbols

k : Thermal conductivity (W/m·°C)
ρ : Density (kg/m³)

Subscripts

b : Building material
m : Melting
s : Surface
Ref : Reference
num : Numerical
exp : Experiment
in : Interior
ext : Exterior

References

[1] Ghedamsi, R. – Settou, N. – Gouareh, A. – Khamouli, A. – Saifi, N. – Recioui, B. (2015): Estimating the energy consumption in building sector in Algeria using bottom-up mode, in: *IEEE 16th International Renewable Energy Congress (IREC),* May 2015, https://doi.org/10.1109/IREC.2015.7110942

[2] Dincer, I. – Rosen, M. (2002): Thermal Energy Storage - Systems and Applications. *John Wiley and Sons*.

[3] Diaconu, M. – Cruceru, M. (2010): Novel concept of composite phase change material wall system for year-round thermal energy savings. *Energy and Buildings*. Vol. 42, No. 10, October 2010, pp. 1759-1772. https://doi.org/10.1016/j.enbuild.2010.05.012

[4] Sharma, A. – Tyagi, V. V. – Chen, C. R. – Buddhi, D. (2009): Review on thermal energy storage with phase change materials and applications. *Renewable and Sustainable Energy Reviews*. Vol. 13, No.2, February 2009, pp.318–345. https://doi.org/10.1016/j.rser.2007.10.005

[5] Abhat, A. (1983): Low temperature latent heat thermal energy storage: Heat storage materials. *Solar Energy*. Vol. 30, No. 4, pp. 313–32. https://doi.org/10.1016/0038-092X(83)90186-X

[6] Lorsch, H. G. – Kauffman, K. W. – Denton, J. C. (1976): Thermal energy storage for heating and air conditioning: future energy production system. *Heat Mass Transfer Proceedings*. Vol. 1, January 1976, pp. 69–81.

[7] Lavinia, S. – Angela, P. – Paula, U. – Oana, G. (2014): Review on phase change materials for building applications. *Leonardo Electronic Journal of Practices and Technologies*. Vol. 13, No. 25, December 2014, pp. 179-194

[8] Jones, B. – Hsieh, K. – Hashinaga, M. (1986): The effect of air velocity on thermal comfort at moderate activity levels. *ASHRAE Transactions*. Vol. 92, 1986, pp. 761–769.

[9] Mondal, S. (2008): Phase change materials for smart textiles-an overview. *Applied Thermal Engineering*. Vol. 28, No. 11–12, August 2008, pp. 1536–1550. https://doi.org/10.1016/j.applthermaleng.2007.08.009

[10] Schossig, P. – Henning, H. M. – Gschwander, S. – Haussmann, T. (2005): Micro-encapsulated phase-change materials integrated into construction materials. *Solar Energy Materials and Solar Cells*. Vol. 89, No. 2–3, November 2005, pp. 297–306. https://doi.org/10.1016/j.solmat.2005.01.017

[11] Farid, M. M. – Khudhair, A. M. – Razack, S. A. K. – Al-Hallaj, S. (2004): A review on phase change energy storage: materials and applications. *Energy Conversion and Management.* Vol. 45, No. 9-10, Jun 2004, pp. 1597–1615. https://doi.org/10.1016/j.enconman.2003.09.015

[12] Raabe, J. – Tzvetkov, G. – Flechsig, U. – Böge, M. – Jaggi, A. – Sarafimov, B. – Vernooij, M. G. C. – Huthwelker, T. – Ade, H. – Kilcoyne, D. – Tyliszczak, T. – Fink, R. H. – Quitmann, C. (2008): PolLux: a new facility for soft X-ray spectromicroscopy at the Swiss Light Source. *Review of Scientific Instruments.* Vol. 79, No.11, November 2008, pp. https://doi.org/10.1063/1.3021472

[13] Oliver, A. – Neila, F. – García, A. (2010): Caracterización térmica de placas de yeso con material de cambio de faseincorporado. *Informes de la construcción.* Vol. 62, No. 519, 2010, pp. 55–66. https://doi.org/10.3989/ic.09.036

[14] Khudhair, A. M. – Farid, M. M. (2004): A review on energy conservation in building applications with thermal storage by latent heat using phase change materials. *Energy Conservation and Management.* Vol. 45, No. 2, January 2004, pp. 263–275. https://doi.org/10.1016/S0196-8904(03)00131-6

[15] Bentz, D. – Turpin, P. R. (2007): Potential applications of phase change materials in concrete technology. *Cement and Concrete Composites.* Vol. 29, No. 7, August 2007, pp.527–532. https://doi.org/10.1016/j.cemconcomp.2007.04.007

[16] Alawadhi, E. M. (2008): Thermal analysis of a building brick containing phase change material. *Energy and Buildings.* Vol. 40, No. 3, 2008, pp. 351–357. https://doi.org/10.1016/j.enbuild.2007.03.001

[17] Khudair, A. M. – Farid, M. M. (2007): A review on energy conservation in building applications with thermal storage by latent heat using phase change materials. *Energy Conversion and Management.* Vol. 45, No. 2, January 2007, pp. 263–275. https://doi.org/10.1016/S0196-8904(03)00131-6

[18] Hawes, D. – Feldman, W. D. (1992): Absorption of phase change materials in concrete. *Solar Energy Materials and Solar Cells.* Vol. 27, No. 2, July 1992, pp. 91–101. https://doi.org/10.1016/0927-0248(92)90112-3

[19] Soaresa N. – Costab J. J. – Gaspar A. R. – Santos P. (2013): Review of passive PCM latent heat thermal energy storage systems towards buildings' energy efficiency, *Energy and Buildings*. Vol. 59, No. 59, April 2013, pp. 82–103. https://doi.org/10.1016/j.enbuild.2012.12.042

[20] Castell, A. – Medrano, M. – Perez, G. – Cabeza, L. (2010): Experimental study of using PCM in brick constructive solutions for passive cooling, *Energy and Buildings.* Vol. 42, No. 4, April 2010, pp. 534-540. https://doi.org/10.1016/j.enbuild.2009.10.022

[21] Alawadhi, E. (2008): Thermal analysis of building brick containing phase change material, *Energy and Buildings*, Vol. 40, No. 3, 2008, pp. 351-357. https://doi.org/10.1016/j.enbuild.2007.03.001

[22] Joulin, A. – Younsi, Z. – Zalewski, L. – Lassue, S. – Rousse, D. R. – Carvot, J. P. (2011): Experimental and numerical investigation of a phase change material: thermal-energy storage and release. *Applied Energy.* Vol. 88, No.7, July 2011, pp. 2454–62. https://doi.org/10.1016/j.apenergy.2011.01.036

[23] Lamberg, P. – Lehtiniemi, R. – Henell, A. M. (2004): Numerical and experimental investigation of melting and freezing process in phase change materials storage, *International Journal of Thermal Sciences.* Vol. 43, No. 3, March 2004, pp. 277-287. https://doi.org/10.1016/j.ijthermalsci.2003.07.001

[24] Karim, L. – Bontemps, A. – Royon, L. (2013): Thermal energy storage and release of a new component with PCM for integration in floors for thermal management of buildings. *Energy and Buildings.* Vol. 63, August 2013, pp.29-35. https://doi.org/10.1016/j.enbuild.2013.03.042

Ref.:
Souci, Youcef Oussama – **Houat**, Samir: *Numerical study of building materials filled by PCM for thermal energy storage*
Építőanyag – Journal of Silicate Based and Composite Materials, Vol. 70, No. 4 (2018), 123–127. p.
https://doi.org/10.14382/epitoanyag-jsbcm.2018.23

Internal thread cutting process improvement based on cutting tools treatment by composite powders in a magnetic field

Jüri OLT ▪ Chair of Biosystems Engineering, Institute of Technology, Estonian University of Life Sciences ▪ jyri.olt@emu.

Viacheslav V. MAKSAROV ▪ Department of Mechanical Engineering, Saint-Petersburg Mining University ▪ maks78.54@mail.ru

Aleksandr I. KEKSIN ▪ Department of Mechanical Engineering, Saint-Petersburg Mining University ▪ keksin.a@mail.ru

Érkezett: 2018. 05. 08. ▪ Received: 08. 05. 2018. ▪ https://doi.org/10.14382/epitoanyag-jsbcm.2018.24

Abstract

This article deals with the subject of using iron and titanium carbide (Fe + TiC) based composite powder for treatment of cutting tools in a magnetic field with the purpose of improving internal thread cutting process. As a result of studies performed by us, it has been established that composite powder grain size influences the condition of the contact surfaces of cutting tool teeth and process efficiency. Also a relationship has been discovered between the changes in internal thread roughness and the condition of thread tap teeth contact surfaces pretreated in a magnetic field by Fe + TiC composite powder having various grain sizes.

Keywords: internal thread, thread cutting, thread surface roughness, thread tap, magnetic-abrasive finishing, tooth contact surfaces condition, composite powder

Kulcsszavak: belső menet, menetfúrás, menet felületi érdessége, menetfúró, mágneses-abrazív felületkezelés, fog kontakt felület minősége, kompozit por

Jüri OLT, DSc.
Professor at Estonian University of Life Sciences. He is Head of Department of Production Engineering from 2005. His main research area are fundamentals of production enginering, materials cutting and design of technological machinery.

Viacheslav MAKSAROV, DSc.
Professor at Saint-Petersburg Mining University. He is Head of Department of Mechanical Engineering from 2012 and Dean of Electromechanical Faculty from 2015. Specializes in the field of dynamics of machining technological systems.

Aleksandr KEKSIN, PhD.
Associate professor at Saint-Petersburg Mining University. Specializes in the field of materials science and technology of construction materials.

1. Introduction

Fatigue breakdown of thread joints operating under dynamic loads causes emergency and unscheduled machine shutdowns, resulting in increased equipment downtime and financial costs. Fatigue breakdown of thread joints is often encountered in practice; therefore, it forces production workers and researches to think over possible ways of solving this problem time and again.

Quite a wide range of design measures intended to increase fatigue resistance is proposed nowadays. Design assurance is a necessary measure; however, it is not sufficient. Technological measures that ensure necessary quality characteristics of mating thread surfaces also play a great role in fatigue strength improvement [4]. For example, Yakushev found out in his studies [15] that forming thread surface roughness with parameter R_a = 0.63 –1.25 μm increases fatigue strength of a thread joint several times as compared to a threaded joint with surfaces roughness parameter R_a = 2.5 – 3.2 μm.

At present, no significant complications arise as the exterior thread surface microrelief is formed. However, internal thread is quite a different story: it is rather difficult to ensure roughness parameter $R_a \leq 1{,}6$ μm on its flanks. It is especially difficult with items made of corrosion resistant materials that are very often used in power engineering. In this regard, the studies performed by these authors are aimed at forming internal thread surfaces in workpieces corrosion resistant materials so that internal thread flanks roughness would be within R_a = 0.63 – 1.25 μm.

The most common process of forming a internal thread profile is the internal thread tapping process [3, 10, 12]. In spite of its popularity, it has significant drawbacks connected with ensuring the quality indicator specified above.

The technological reduction of internal thread surface roughness Ra < 1.6 μm during tapping is inseparably associated to the improvement of the condition of cutting tool teeth contact surfaces that can be effected by performing finishing operations. Magnetic-abrasive finishing (MAF) [6, 7] is a promising method of forming various conditions (rounding radius, roughness and microhardness) of tooth contact surfaces of a thread tap.

Magnetic-abrasive finishing [1, 5, 13-14, 17] is essentially abrasive effect made of a workpiece (a thread tap) (*Fig. 1*) by ferromagnetic powder abrasive mass compacted by magnetic field [6-9, 11, 16]. Using MAF as final machining of thread taps allows to remove the previous defective layer and to form a new, hardened one, to round off the cutting edges to the necessary limits, as well as to reduce the roughness of cutting teeth contact surfaces in a relatively short space of time (t = 60 – 210 s). As an example, it is presented in *Fig. 2* photographs of contact surfaces of a thread tap teeth before and after magnetic-abrasive finishing [7].

A substantial change in the condition of thread tap teeth contact surfaces is caused by specific features of magnetic-abrasive finishing, namely oriented and selective abrasive microcutting and microsmoothing [7]. Magnetic-abrasive powder having a high cutting power and enhanced magnetic properties plays a major role in microcutting and microsmoothing. However, it is not possible to ensure them at the same time for grains of a homogeneous material. Therefore, the sphere of application of magnetic-abrasive powders made of homogeneous materials is limited to machining of soft materials. It is possible to attain high hardness and good magnetic properties by creating powder materials in which every grain is a composition from ferromagnetic base and hard non-magnetic inclusions.

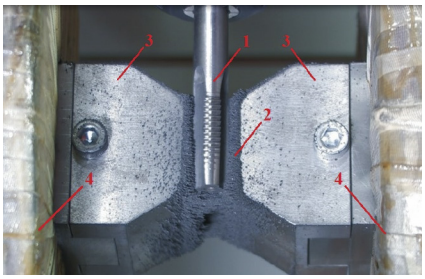

Fig. 1. Magnetic-abrasive finishing of a thread tap: 1) – the tap; 2) – magnetic-abrasive powder; 3) – pole tips; 4) – solenoids.
1. ábra Menetfúró mágneses-abrazív felületkezelése: 1) fúrószerszám, 2) mágneses-abrazív por, 3) elektródavégek, 4) tekercsek

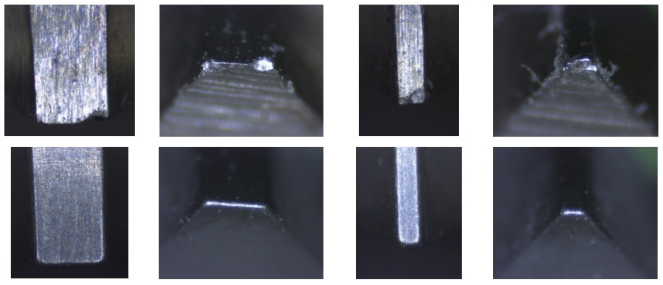

a) b)

Fig. 2. Thread tap teeth before (the upper row) and after (the lower row) magnetic-abrasive finishing: a and b) the 4th tooth at the inlet section; c and d) the 6th tooth at the calibrating section
2. ábra Menetfog a mágneses-abrazív felületkezelés előtt (felső sor) és után (alsó sor): a és b) a negyedik fog a beömlési szelvényben, c és d) a hatodik fog a kalibrálási szelvényben

The most efficient composite magnetic-abrasive powder is a composite based on iron and titanium carbide (Fe + TiC) [1], a final product of chemical interaction resulting from combined heating of mixtures Fe + C + Ti. The presence of iron in the process of synthesis does not impede generation of titanium carbide in the temperature range from 1400 to 1600 °C. However, a rise in temperature brings about a reduction in titanium carbides content in the composition because of their dissolution [1].

Analysis of the Fe + TiC composite powder microstructure (*Fig. 3.a*) demonstrates that dark rounded spots (globules) of titanium carbides are observed against the light background of iron matrix. The globules differ in size insignificantly; they are distributed evenly throughout the matrix field. The size of the globules depends on the carbide phase concentration in the composition, i.e. grains grow larger as carbide concentration increases. The rounding of globules is caused by a limited capacity of titanium carbides dissolution in iron and the striving of every system to take the form that is the most suitable for it [1].

Powder particles are shaped as irregular polyhedrons (*Fig. 3.c*) with protruding carbide grains being abrasive cutting areas. The surface morphology of a high-melting abrasive in ferromagnetic matrix, its size and shape are presented in *Fig. 3.b*.

The microstructure of powder consists of carbides in the form of spherical, flakey and cast inclusions in iron matrix. The microhardness of ferromagnetic matrix is within the range of 2,100 – 3,400 MPa and that of Ti-C is 30,000 – 31,000 MPa. High microhardness of titanium carbide, a low level of its interaction with iron at high heating temperatures and, as a consequence, good magnetic properties of powder allow to ensure intense removal of base metal and an improved quality of the machined surface [1].

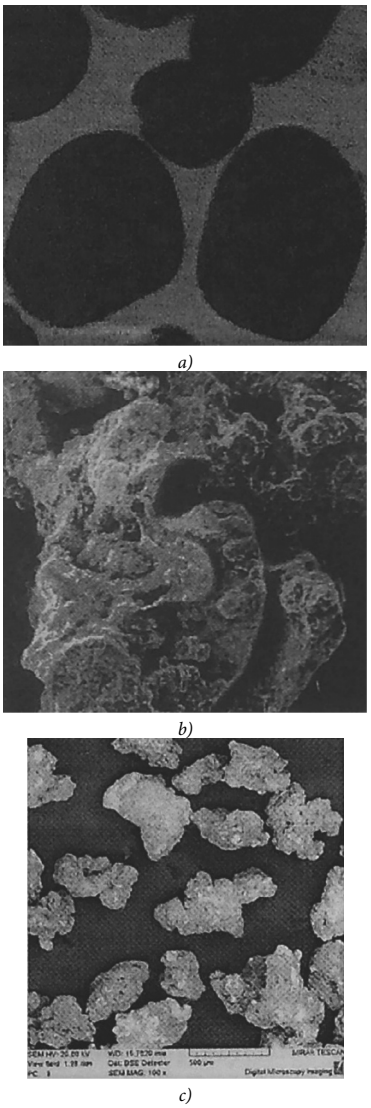

a) b) c)

Fig. 3. Composite magnetic-abrasive powder based on iron and titanium carbide (Fe + TiC): a) powder microstructure; b) particle morphology; c) the shape of grains [1]
3. ábra Vas és titánkarbid (Fe + TiC) alapú kompozit mágneses-abrazív por: a) por mikroszerkezet, b) szemcse morfológia, c) szemcsealak [1]

Thus, the purpose of the studies carried out by these authors is to improve the internal thread tapping technology through preliminary treatment of the thread tap using the MAF method with the help of Fe + TiC composite powder.

2. Materials and experimental methods

The magnetic-abrasive finishing of the thread tap was carried out on a specially designed plant located in the CNC machines laboratory at the department of mechanical engineering of the Saint Petersburg Mining University. The MAF device was based on a CNC milling machine that provides all working movements necessary for the machining process.

M16×2 thread taps made of R6M5 quick-cutting steel were taken as pilot prototypes. A composite powder based on iron and titanium carbide (Fe + TiC) having various grain sizes Δ = 160 – 315 μm was used for forming a magnetic-abrasive brush in the work zone of the electromagnetic system. The following constant process factors were adopted for the magnetic-

abrasive finishing of the thread taps: magnetic flux density B = 0.6 T; polishing time t = 210 s; the thread tap rotation frequency in the work space of the electromagnetic system n = 475 rpm; thread tap advance along the pole tips S = 120 mm/min; machining gap between the pole tips and the thread tap δ = 1 mm. The following parameters were used to control the condition of the contact surfaces of the thread tap teeth: cutting edge rounding radius ρ, μm; roughness of the flanks, the front and the rear surfaces of the cutting teeth Ra_1, Ra_2 and, respectively Ra_3, μm; microhardness of the rear surfaces of teeth HV, MPa; the amount of material being removed Q, g.

The rounding radius of the cutting edges, the roughness of the flanks, the front and the rear surfaces of the thread tap cutting teeth were controlled with the help of a Hommel Tester T8000 profilograph-profilometer; microhardness was measured with the help of a PMT-3M microhardness tester; the amount of removed material, with the help of a VLTE 310 type scale.

The studies of internal thread cutting technology were carried out using a Trens SN 32/750 thread-cutting lathe. The workpieces undergoing the machining were made of 08Kh18N10T grade corrosion resistant material (metal thickness 40 mm). M16×2 mm thread taps were taken as cutting tools. Theses taps were preliminarily subjected to MAF with the purpose of creating various conditions of the contact surfaces of the tool teeth.

After cutting internal thread in a workpiece made of a corrosion resistant material using thread taps preliminarily subjected to MAF under various machining conditions, the roughness of the flanks of the internal thread profile was controlled. Roughness was controlled using a Hommel Tester T8000 profilograph-profilometer.

The experimental data on the roughness of internal thread surfaces were subjected to statistical analysis in the Statistica 10 software environment.

3. Results and discussion

As a result of the studies of magnetic-abrasive finishing of thread taps using Fe + TiC composite powder, it has been established that the magnetic-abrasive powder grain size Δ influences the condition of thread tap teeth contact surfaces, characterized by the cutting edge rounding radius ρ, the roughness of the cutting teeth flanks Ra_1, that of their front Ra_2 and rear Ra_3 surfaces, the microhardness of cutting teeth rear surfaces Hv, and at the machining efficiency expressed in the amount of removed material Q (*Fig. 4*).

Analysis of the dependency curves presented in *Fig. 4* allows to conclude that within the range of Fe + TiC composite powder grain sizes under study (Δ = 160 – 315 μm), the thread tap cutting edges rounding radius after MAF varies within the range ρ = 40…51 μm, the roughness of tooth flanks Ra_1 = 0,068…0,073 μm, the roughness of tooth front surfaces Ra_2 = 0.09 – 0.11 μm, the roughness of tooth rear surfaces Ra_3 = 0,095…0,149 μm, the microhardness of tooth rear surfaces Hv = 9,722 – 11,162 MPa and the amount of removed material is within the range Q = 6…8 g.

The studies of thread taps MAF with the use of Fe + TiC composite powder having various grain size bear witness to a substantial improvement of the condition of cutting tool teeth contact surfaces in view of the fact that originally the cutting edge had defects resulting from previous machining (*Fig. 2*), the tooth flank roughness was equal to R_{a1} = 0,19 μm, the tooth front surface roughness R_{a2} = 0,26 μm, the tooth rear surface roughness Ra_2 = 0,26 μm and the tooth rear surface microhardness Hv = 7,507 MPa.

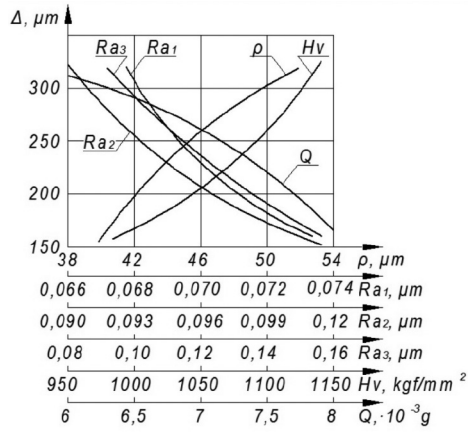

Fig. 4. Fe + TiC composite powder grain size vs. the condition of thread tap teeth contact surfaces and the MAF efficiency curves: ρ – cutting edge rounding radius; R_{a1} – tooth flank roughness; R_{a2} – tooth front surface roughness; R_{a3} – tooth rear surface roughness; Hv – rear tooth surface microhardness; Q – the amount of removed material

4. ábra Fe + TiC kompozit por szemcseméret és a fúrószerszám kontak felületének állapota, MAF hatékonysági görbék: ρ – vágóél lekerekítési rádiusz; R_{a1} – fog profil érdesség; R_{a2} – fog frontfelület érdessége; R_{a3} – fog hátfelület érdessége; Hv – fog hátfelület mikrokeménysége; Q – leválasztott anyagmennyiség

After the MAF of thread taps using Fe + TiC composite powder, experimental studies of internal thread cutting were performed. The thread taps used in this studies were previously machined by composite powder having various grain sizes in a magnetic field, and a dependency has been established between a change in internal thread roughness and the condition of thread tap teeth contact surfaces. Since condition is understood as a totality of microgeometrical parameters of contact surfaces of teeth, i.e. the cutting edge rounding radius, the roughness of cutting teeth flanks, front and rear surfaces, the microhardness of teeth rear surfaces and it is not possible to detect the dependency between the influence of each of these parameters on the internal thread roughness since during the MAF they are formed simultaneously, it was decided to plot the dependency curve in the following way: plot the thread roughness values on the ordinate axis and the composite powder grain size values that changed during forming of various conditions of thread tap teeth contact surfaces during the MAF, on the abscissa axis.

The dependency between changes in internal thread roughness and the condition of thread tap teeth contact surfaces presented in *Fig. 5* allows to conclude that an increase in composite powder grain size from 160 to 315 μm during the MAF of thread taps is accompanied in the subsequent process of internal thread cutting using these taps by increased roughness of the profile of internal thread cut in workpieces made of 08Kh18N10T grade corrosion resistance material from 0.85 to 1.28 μm (Ra parameter). It should be noted that the roughness of internal thread cut by a thread tap that was not previously subjected to the MAF is 1.77 μm. The roughness of thread cut

by a previously MAF machined thread tap is reduced at least 1.4 times irrespective of composite powder grain size Δ = 160 – 315 μm. This confirms the efficiency of using this finishing method within the framework of the parameters range under study.

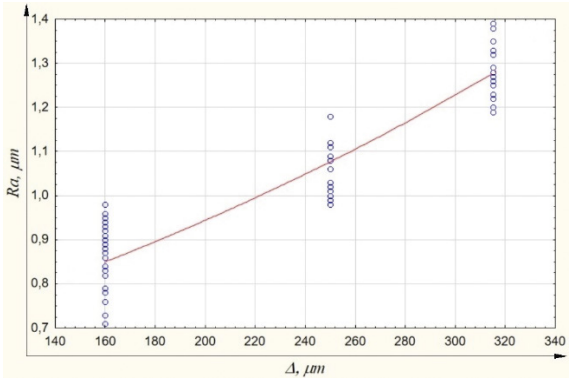

Fig. 5. Dependency between changes in internal thread roughness (Ra) and the condition of thread tap teeth contact surfaces formed due to varying composite powder grain size

5. ábra Kompozit por szemcseméretének hatása a fúrószerszám fog kontakt felületének állapota és a belső menet felületi érdessége (Ra) közötti kapcsolatra

The studies of the MAF of thread taps using Fe + TiC having various grain size have shown that thread tap cutting edges rounding radius changes within the range of ρ = 40 – 51 μm (*Fig. 4*). Since the cutting depth during thread tapping a < ρ, in this case the deterioration of internal thread roughness R_a parameter in workpieces made of 08Kh18N10T grade corrosion resistant material from 0.85 to 1.25 μm can be explained by elastic deformation of a workpiece surface layer in the process of cutting that has an adverse effect on surface microrelief formation.

Experimental data analysis allowed to conclude that within the Fe + TiC composite powder grain size range under study (Δ = 160 – 315 μm) the most efficient MAF method for thread taps machining is using powder grain size Δ = 160 μm at magnetic flux density B = 0.6 T and finishing time t = 210 s.

4. Conclusions

In conclusion, it can be said that using magnetic-abrasive finishing (MAF) during the machining of thread taps for the improvement of technology of internal thread surface cutting in workpieces made of 08Kh18N10T grade corrosion resistant material will allow to reduce the roughness of internal thread surfaces from Ra = 1.77 μm (thread cutting by a standard thread tap) to Ra = 1.28 – 0.85 μm (depending on the Fe + TiC composite powder grain size used during the MAF of thread taps).

Thus, the purpose of studies set by the authors (improvement of internal thread cutting technology by means of preliminary MAF of thread tap teeth contact surfaces) can be considered as achieved since internal thread profile flank roughness Ra < 1.6 μm and within the range of Ra = 0.63 – 1.25 μm in workpieces made of a corrosion resistant material is ensured.

References

[1] Akulovich, L. M. – Sergeev, L. E. – Lebedev, V. Y. (2012): Fundamentals of magnetic-abrasive finishing of metal surfaces. BGATU, Minsk, 316 p.

[2] Boldyrev, I. S. (2015): Simulation of thread cutters with manufacturing errors. *Russian Engineering Research*, Vol. 35, Issue 5, 18 May 2015, pp. 375-377, https://doi.org/10.3103/S1068798X1505007X

[3] Cao, T. – Sutherland, J. W. (2002): Investigation of thread tapping load characteristics through mechanistic modeling and experimentation. *International Journal of Machine Tools and Manufacture*. Vol. 42, Issue 14, November 2002, pp. 1527–1538, https://doi.org/10.1016/S0890-6955(02)00108-6

[4] Fedorova, L. V. – Ivanova, Y. S. – Voronina, M. V. (2017): Improvement of thread joint reliability by means of electromechanical processing. *Journal of Mining Institute*, Vol. 266, pp. 456-461.

[5] Guo, J. – Tan, Z. E. E. – Au, K. H. – Liu, K. (2017): Experimental investigation into the effect of abrasive and force conditions in magnetic field-assisted finishing. International Journal of Advanced Manufacturing Technology, Vol. 90, Issue 5-8, pp. 1881-1888, https://doi.org/10.1007/s00170-016-9491-6

[6] Maksarov, V. V. – Keksin, A. I. (2013): Methods of increasing the quality of thread pitches. *Agronomy Research*. Vol. 11 No. 1, May 2013, pp. 133-138.

[7] Maksarov, V. V. – Keksin, A. I. (2017): Technological improvement of complex surfaces quality by magnetic-abrasive finishing. *Metalloobrabotka*. Vol. 97, No. 1, pp. 47-57.

[8] Misra, A. M. – Pandey, P. – Dixit, U. S. (2017): Modeling of material removal in ultrasonic assisted magnetic abrasive finishing process. *International Journal of Mechanical Sciences*, Vol. 131-132, October 2017, pp. 853-867, https://doi.org/10.1016/j.ijmecsci.2017.07.023

[9] Nguyen, N. – Tran, T. – Yin, S. – Chau, M. – Le, D. (2017): Multi-objective optimization of improved magnetic abrasive finishing of multi-curved surfaces made of SUS202 material. *International Journal of Advanced Manufacturing Technology*, Vol. 88, Issue 1-4, January 2017, pp. 381-391, https://doi.org/10.1007/s00170-016-8773-3

[10] Pereira, I. C. – da Silva, M. B. (2017): Study of the internal thread process with cut and form taps according to secondary characteristics of the process. *International Journal of Advanced Manufacturing Technology*, Vol. 93, Issue 5-8, Nov. 2017, pp. 2357-2368, https://doi.org/10.1007/s00170-017-0573-x

[11] Rodriguez, C. J. (2009): Cutting edge preparation of precision cutting tools by applying micro-abrasive jet machining and brush. *Kassel University Press GmbH*, Kassel, 205 p.

[12] Tanaka, R. – Yamazaki, S. – Hosokawa, A. – Furumoto, T. – Ueda, T. – Okada, M. (2013): Analysis of Cutting Behavior during Tapping and Measurement of Tool Edge Temperature Measured by a Two-Color Pyrometer. *Journal of Advanced Mechanical Design, Systems, and Manufacturing*. Vol. 7, Issue 2, pp. 115–124, https://doi.org/10.1299/jamdsm.7.115

[13] Verma, G. C. – Kala, P. – Pandey, P. M. (2017): Experimental investigations into internal magnetic abrasive finishing of pipes. *International Journal of Advanced Manufacturing Technology*, Vol. 88, Issue 5-8, pp. 1657-1668, https://doi.org/10.1007/s00170-016-8881-0

[14] Wu, J. – Zou, Y. – Sugiyama, H. (2016): Study on finishing characteristics of magnetic abrasive finishing process using low-frequency alternating magnetic field. *International Journal of Advanced Manufacturing Technology*, Vol. 85, Issue 1-4, 1 July 2016, pp. 585-594, https://doi.org/10.1007/s00170-015-7962-9

[15] Yakushev, A. I. – Mustaev, R. K. – Mavlyutov, R. R. (1979): Increasing strength and reliability thread joint. Mashinostroenie, Moscow, 215 p.

[16] Yin, S. – Shinmura, T. (2004): Vertical vibration-assisted magnetic abrasive finishing and deburring for magnesium alloy. *International Journal of Machine Tools and Manufacture*. Vol. 44, No. 12-13, Oct. 2004, pp. 1297-1303, https://doi.org/10.1016/j.ijmachtools.2004.04.023

[17] Zhang, X. – Li, W. – Hou, Z. – Li, W. (2017): Experiment on Magnetic Abrasive Finishing for Quartz Glass. *Nami Jishu yu Jingmi Gongcheng/ Nanotechnology and Precision Engineering*, Vol. 15, Issue 4, pp. 261-266, https://doi.org/10.13494/j.npe.20160092

Ref.:
Olt, Jüri – **Maksarov**, Viacheslav V. – **Keksin**, Aleksandr I.: *Internal thread cutting process improvement based on cutting tools treatment by composite powders in a magnetic field*
Építőanyag – Journal of Silicate Based and Composite Materials, Vol. 70, No. 4 (2018), 128–131. p.
https://doi.org/10.14382/epitoanyag-jsbcm.2018.24

GUIDELINE FOR AUTHORS

The manuscript must contain the followings: title; author's name, workplace, e-mail address; abstract, keywords; main text; acknowledgement (optional)**; references; figures, photos with notes; tables with notes; short biography** (information on the scientific works of the authors).

The full manuscript should not be more than 6 pages including figures, photos and tables. Settings of the word document are: 3 cm margin up and down, 2,5 cm margin left and right. Paper size: A4. Letter size 10 pt, type: Times New Roman. Lines: simple, justified.

TITLE, AUTHOR

The title of the article should be short and objective.

Under the title the name of the author(s), workplace, e-mail address.

If the text originally was a presentation or poster at a conference, it should be marked.

ABSTRACT, KEYWORDS

The abstract is a short summary of the manuscript, about a half page size. The author should give keywords to the text, which are the most important elements of the article.

MAIN TEXT

Contains: materials and experimental procedure (or something similar), results and discussion (or something similar), conclusions.

REFERENCES

References are marked with numbers, e.g. [6], and a bibliography is made by the reference's order. References should be provided together with the DOI if available.

Examples:

Journals:

[6] Mohamed, K. R. – El-Rashidy, Z. M. – Salama, A. A.: In vitro properties of nano-hydroxyapatite/chitosan biocomposites. *Ceramics International.* 37(8), December 2011, pp. 3265–3271, http://doi.org/10.1016/j.ceramint.2011.05.121

Books:

[6] Mehta, P. K. – Monteiro, P. J. M.: Concrete. Microstructure, properties, and materials. *McGraw-Hill*, 2006, 659 p.

FIGURES, TABLES

All drawings, diagrams and photos are figures. The **text should contain references to all figures and tables**. This shows the place of the figure in the text. Please send all the figures in attached files, and not as a part of the text. **All figures and tables should have a title**.

Authors are asked to submit color figures by submission. Black and white figures are suggested to be avoided, however, acceptable.

The figures should be: tiff, jpg or eps files, 300 dpi at least, photos are 600 dpi at least.

BIOGRAPHY

Max. 500 character size professional biography of the author(s).

CHECKING

The editing board checks the articles and informs the authors about suggested modifications. Since the author is responsible for the content of the article, the author is not liable to accept them.

CONTACT

Please send the manuscript in electronic format to the following e-mail address: femgomze@uni-miskolc.hu and epitoanyag@szte.org.hu or by post: Scientific Society of the Silicate Industry, Budapest, Bécsi út 122–124., H-1034, HUNGARY

We kindly ask the authors to give their e-mail address and phone number on behalf of the quick conciliation.

Építőanyag – *Journal of Silicate Based and Composite Materials*, Quarterly peer-reviewed periodical of the Hungarian Scientific Society of the Silicate Industry, SZTE.
http://epitoanyag.org.hu

BUILDING MATERIALS 2019

Euro Building Materials & Construction Technologies Conferences

June 20-21, 2019 | Stockholm, Sweden

About Conference

The fundamental subject of Building Materials & Construction Technologies 2018 is "Commencing New Techniques for Efficient Structures & Dwellings". This unique opportunity that we extend to our speakers and attendees is not being offered by any other conference organizers. Through this the abstracts and research profiles of our speakers and organizing committee members getting global visibility which is an additional feature that you would be receiving in addition to networking opportunities before, during and after the conference.

BUILDING MATERIALS 2019 salient features

- Meet Academia and Industry visionaries to get inspired
- Expand your knowledge and find solutions to problems
- Knowledge, Benchmarking and Networking offered at one place
- Forge connections and for global networking
- Highly Organized and Structured Scientific programs
- Poster presentations and world class exhibitions
- Meet with new vendors and suppliers

How Conference Series LLC Ltd Conferences differs from others?

- 3000+ Conferences across the globe in 30+ countries all through the year
- Over 25 Million+ Visitors and 20000+ Unique Visitors per conference
- Participation by Stalwarts from various international societies
- Internationally renowned speakers and scientists representation
- Career guidance for early career researchers and students
- Interesting scientific deliberations and discussions
- Perfect platform for Global Networking

Goals

- The conference program emphasizes evidence-based practice, educational innovation, practical application, and peer to peer networking and collaboration. The goals of the conference is to provide a transformative professional development experience through
- Bringing together the world's scientific experts to catalyze and advance scientific knowledge about Building Materials & Construction Technology new techniques, and promote and enhance scientific collaborations around the world.
- Bringing together community leaders, scientists, and policy leaders to promote and enhance the knowledge towards improving the material both durable and economical. Thereby reducing the risk factor for living beings.

Objectives

- After participating in this meeting, attendees should be able to
- Discuss emerging issues in new Building Material techniques
- Discuss and apply recent research findings related to Eco-friendly building materials
- Reflect on the place of critical distance in Building Materials & Construction Technologies

Major Sessions

- Durability Enhancing Products
- Recycled Aggregates
- Green Building Materials
- Sustainable Construction
- Waste Reduction
- Biodegradable waste
- Structural Loads
- Load Cases
- Design of Shear Walls
- Plans for urban and rural subdivisions
- Determining & implementing zoning laws
- Elastic deformation
- Chemical Reaction
- Plant & Equipment management
- Infamous disasters in engineering
- Bearing capacity of Soil
- Bridge Launching Techniques



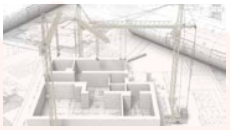


Theme: Commencing New Techniques for Efficient Structures & Dwellings

Organized by the
Italian Ceramic Society
www.icers.it - info@icers.it

societa' ceramica italiana

XVI ECerS CONFERENCE

TORINO
16-20 JUNE
2019

XVI CONFERENCE AND EXHIBITION OF THE EUROPEAN CERAMIC SOCIETY

www.ecers2019.org

Organizing Secretariat

AIM GROUP INTERNATIONAL

AIM Group International
Florence Office
info@ecers2019.org